JOURNAL OF PETROLOGY | VOLUME 47 | NUMBER 11 | PAGES 2257–2279 | 2006 | doi:10.1093/petrology/egl043

Cyclicity in the Main and Upper Zones of the Bushveld Complex, South Africa: Crystallization from a Zoned Magma Sheet

CHRISTIAN TEGNER[1]*, R. GRANT CAWTHORN[2] AND F. JOHAN KRUGER[3]

[1]DEPARTMENT OF EARTH SCIENCES, AARHUS UNIVERSITY, C. F. MØLLERS ALLÉ 110, DK-8000 AARHUS C, DENMARK

[2]SCHOOL OF GEOSCIENCES, UNIVERSITY OF THE WITWATERSRAND, P.O. WITS 2050, SOUTH AFRICA

[3]MORUO MINERALOGICAL SERVICES, P.O. BOX 1368, KRUGERSDORP, 1740, SOUTH AFRICA

**RECEIVED JANUARY 17, 2006; ACCEPTED JULY 28, 2006;
ADVANCE ACCESS PUBLICATION SEPTEMBER 6, 2006**

The major element composition of plagioclase, pyroxene, olivine, and magnetite, and whole-rock $^{87}Sr/^{86}Sr$ *data are presented for the uppermost 2·1 km of the layered mafic rocks (upper Main Zone and Upper Zone) at Bierkraal in the western Bushveld Complex. Initial* $^{87}Sr/^{86}Sr$ *ratios are near-constant (0·7073 ± 0·0001) for 24 samples and imply crystallization from a homogeneous magma sheet without major magma recharge or assimilation. The 2125 m thick section investigated in drill core comprises 26 magnetitite and six nelsonite (magnetite–ilmenite–apatite) layers and changes up-section from gabbronorite (*An_{72} *plagioclase; Mg# 74 clinopyroxene) to magnetite–ilmenite–apatite–fayalite ferrodiorite (*An_{43}*; Mg# 5 clinopyroxene;* Fo_1 *olivine). The overall fractionation trend is, however, interrupted by reversals characterized by higher An% of plagioclase, higher Mg# of pyroxene and olivine, and higher* V_2O_5 *of magnetite. In the upper half of the succession there is also the intermittent presence of cumulus olivine and apatite. These reversals in normal fractionation trends define the bases of at least nine major cycles. We have calculated a plausible composition for the magma from which this entire succession formed. Forward fractional crystallization modeling of this composition predicts an initial increase in total iron, near-constant* SiO_2 *and an increasing density of the residual magma before magnetite crystallizes. After magnetite begins to crystallize the residual magma shows a near-constant total iron, an increase in* SiO_2 *and decrease in density. We explain the observed cyclicity by bottom crystallization. Initially magma stratification developed during crystallization of the basal gabbronorites. Once magnetite began to crystallize, periodic density inversion led to mixing with the overlying magma layer, producing mineralogical breaks between fractionation cycles. The magnetitite and nelsonite layers mainly occur within fractionation cycles, not at their bases. In at least two cases, crystallization of thick magnetitite layers may have lowered the density of the basal layer of melt dramatically, and triggered the proposed density inversion, resulting in close, but not perfect, coincidence of mineralogical breaks and packages of magnetitite layers.*

KEY WORDS: *layered intrusion; mineral chemistry; isotopes; magma; convection; differentiation*

INTRODUCTION

The ~6·5 km thick sequence of ultramafic and mafic rocks of the Bushveld Complex is the largest layered mafic intrusion known on Earth and it crops out in three major areas (limbs) in northern South Africa (Fig. 1). Interpretation of gravity data suggests that the eastern and western limbs are connected over at least 65 000 km^2 (Cawthorn & Webb, 2001); thus the intrusion can be considered as a large igneous province in its own right (Coffin & Eldholm, 1994). The intrusion was emplaced into the upper crust at about 2·06 Ga (Buick *et al.*, 2001) in several major magma recharge events (Cawthorn & Walraven, 1998) and it hosts some of the world's largest and richest orthomagmatic metal deposits (Lee, 1996; Cawthorn *et al.*, 2005). The final major magma recharge event took place in the Main Zone (Fig. 2) about 4·2 km up in the stratigraphy and resulted in lateral expansion

---

*Corresponding author. E-mail: christian.tegner@geo.au.dk

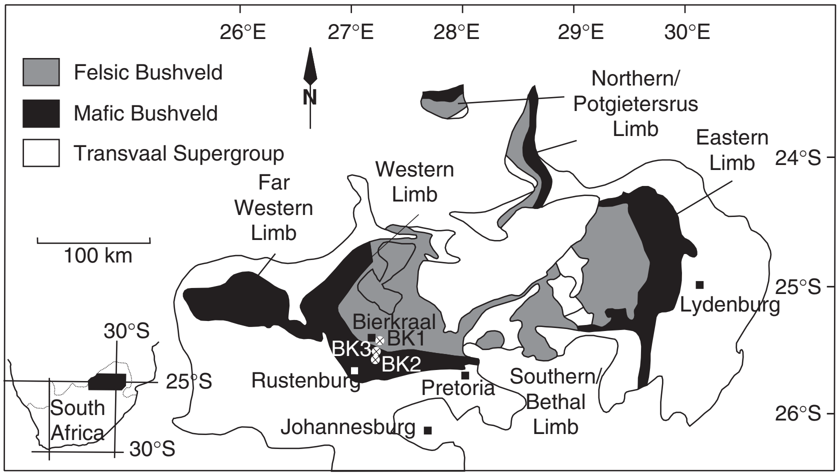

Fig. 1. Map of the Bushveld Complex showing the location of the Bierkraal drill holes, BK1, BK2 and BK3. Modified after Lundgaard *et al.* (2006).

of the sheet-like magma chamber (Kruger, 2005). Evidence for mixing at this level between residual and recharged magma comes from protracted reversals in Mg# and An contents of pyroxene and plagioclase, and changes in initial $^{87}Sr/^{86}Sr$ value. Within this interval a distinct, thin layer of orthopyroxenite occurs, known as the Pyroxenite Marker, which is present in both the eastern (von Gruenewaldt, 1970) and western limbs (Cawthorn *et al.*, 1991). The initial $^{87}Sr/^{86}Sr$ composition of the ~2·1 km thick cumulate sequence above the Pyroxenite Marker, which comprises the upper Main Zone (MZ_U) and the Upper Zone (UZ) (Fig. 2), is constant with an average of 0·7073 ± 0·0001 (2 standard error; S.E.) and significantly different from the underlying 4·2 km of cumulates (Kruger *et al.*, 1987; Kruger, 1994). This has been explained by complete homogenization between residual and added magma above the Pyroxenite Marker (Kruger *et al.*, 1987; Cawthorn *et al.*, 1991). With an estimated volume of ~140 000 km^3, the MZ_U and UZ represent the largest known sheet of basaltic magma emplaced into the Earth's crust.

This contribution aims to decipher the physical processes of crystallization within the huge MZ_U and UZ magma sheet. The UZ includes about 30 distinct magnetitite and nelsonite (magnetite–ilmenite–apatite) layers, which vary from 2 to 710 cm thick, and hosts world-class deposits of V, Ti, and P (Cawthorn & Molyneux, 1986; von Gruenewaldt, 1993; Lee, 1996; Cawthorn *et al.*, 2005). From bottom to top, MZ_U and UZ evolve from gabbronorite (Mg# of clinopyroxene is 74) to iron-rich apatite–magnetite–fayalite ferrodiorite (Mg# of clinopyroxene is <5); this sequence has, traditionally, been interpreted as the result of closed-system crystallization without magma recharge (Wager & Brown, 1968; Willemse, 1969*a*, 1969*b*; von Gruenewaldt, 1973; Molyneux, 1974). Several excursions from simple,

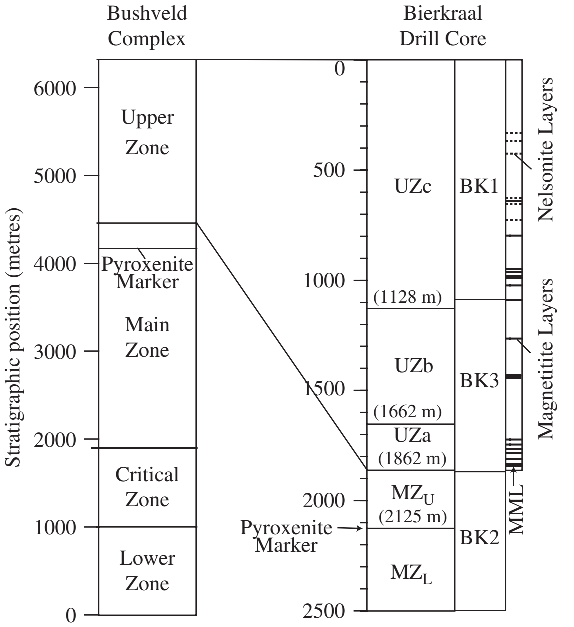

Fig. 2. Generalized stratigraphic section of the Bushveld Complex (left) and the combined Bierkraal drill cores (right). The bases of subzones in the Bierkraal cores delineate the lowest appearance of cumulus magnetite (UZa), olivine (UZb), and apatite (UZc), respectively. The correlations between the three Bierkraal drill cores are: 1600 m depth in BK1 equals 550 m depth in BK3; 1420 m depth in BK3 equals 200 m depth in BK2 [see core logs given by Kruger *et al.* (1987)]. An inferred stratigraphic position in the Bierkraal cores is calculated assuming the core is vertical, that layering dips 24° to the north and that the roof contact is at 415 m depth in BK1. Previous publications on BK drill cores quote only absolute depths below surface. To facilitate comparison with our inferred stratigraphic positions, the following conversion equations have been used: BK1: inferred stratigraphic position in metres = (depth in BK1 – 415) × cos 24°; BK2: inferred stratigraphic position in metres = (depth in BK2 + 1840) × cos 24°; BK3: inferred stratigraphic position in metres = (depth in BK3 + 635) × cos 24°. MML, Main Magnetitite Layer. Modified after Kruger *et al.* (1987).

up-section fractionation trends have, however, been described and different interpretations presented. Merkle & von Gruenewaldt (1986), for example, interpreted changes in pentlandite and olivine compositions to result from magma recharge and mixing. Eales & Cawthorn (1996) showed that the V_2O_5 content of magnetite increases up-section in at least one interval and noted that this could not be explained by changes in intensive parameters, such as fO_2, during fractional crystallization. Likewise, Ashwal *et al.* (2005) documented reversals in the Mg# of pyroxene and An% of plagioclase in a drill core through the MZ_U and UZ in the northern limb that were interpreted as evidence for magma recharge. Many studies of the UZ have focused on the petrogenesis of the magnetitite layers (Bateman, 1951; Wager & Brown, 1968; Irvine, 1975; Cawthorn & McCarthy, 1980; Klemm *et al.*, 1985; Reynolds, 1985*a*; von Gruenewaldt *et al.*, 1985; Kruger & Smart, 1987; Harney *et al.*, 1990, 1996; von Gruenewaldt, 1993). Interpretations vary and will be discussed in detail below.

Here we present new major element data for plagioclase, clinopyroxene, olivine and orthopyroxene, V_2O_5 in magnetite, and whole-rock Sr isotope data for the 2·1 km thick section of MZ_U and UZ sampled in the Bierkraal drill cores of the western limb (Fig. 1). With the exception of one drill core in the northern limb (Ashwal *et al.*, 2005), there is a dearth of systematic electron microprobe data for silicate minerals in the upper part of the Bushveld Complex. The new data, together with published P_2O_5 bulk-rock data for the same drill core (Cawthorn & Walsh, 1988), demonstrate pronounced cycles in mineral compositions, V_2O_5 in magnetite, and the intermittent presence of apatite and olivine. To help explain the genesis of these cycles and the formation of magnetitite and nelsonite layers, we developed a forward crystallization model that predicts the liquid line of descent, the magma density and instantaneous equilibrium mineral compositions during crystallization of the MZ_U and UZ.

PETROLOGY AND GEOCHEMISTRY OF THE MAIN AND UPPER ZONES

Zonal subdivision

Subdivisions of layered intrusions are normally based on the appearance and disappearance of cumulus minerals, and hence, in principle, should be identifiable in the field (Wager & Brown, 1968). Divisions based on more sophisticated and geochemical criteria, such as stratigraphic changes in Sr isotope ratios in the case of the Bushveld Complex, may make genetic sense, but are not easily implemented. Here we will focus only on the criteria for subdividing the Main and Upper Zones (Fig. 2). In the upper part of the Main Zone in the eastern limb, von Gruenewaldt (1970) identified a thin orthopyroxenite layer known as the Pyroxenite Marker. Below this level, the rocks contain original pigeonite, now inverted to orthorhombic pyroxene with abundant exsolution, and are referred to as the lower Main Zone (MZ_L). The Pyroxenite Marker and overlying rocks contain primary orthopyroxene. A similar pyroxenite layer, and associated pyroxene phase changes, has also been identified in the western limb (Cawthorn *et al.*, 1991). Several further studies have confirmed the lateral continuity of these mineralogical successions in both limbs (Mitchell *et al.*, 1998; Nex *et al.*, 1998; Lundgaard *et al.*, 2006). Through an interval of about 200 m the Pyroxenite Marker is also associated with a gradual upward increase in An% in plagioclase and Mg# in pyroxene and a change in initial $^{87}Sr/^{86}Sr$ (Sr_0) from 0·7082 below to 0·7073 above, demonstrating that the Pyroxenite Marker formed as a consequence of magma recharge and mixing (Kruger *et al.*, 1987; Cawthorn *et al.*, 1991). Following the long established terminology for the Bushveld Complex (Wager & Brown, 1968), we to refer to the rocks immediately above the Pyroxenite Marker as the upper Main Zone (MZ_U) (Fig. 2).

Willemse (1969*a*, 1969*b*) used the Main Magnetitite Layer (Fig. 2) to define the base of the Upper Zone (UZ). In contrast, von Gruenewaldt (1973) suggested that the UZ was composed of four subzones, with the base of the lowest, subzone UZa, being taken as the first appearance of cumulus magnetite. The base of subzone UZb was placed at the base of the Main Magnetitite Layer and the appearance of olivine and apatite defined the bases of subzones UZc and UZd, respectively. We have certain reservations about these schemes. The ~2·5 m thick Main Magnetitite Layer is certainly an excellent marker in the field. However, because the cumulus mineralogy does not change across this layer, we question whether it should be used as a zonal or subzonal boundary. Using cumulus mineralogical criteria, we suggest instead a three-fold subdivision, following Wager & Brown (1968), based on the lowest appearance of magnetite (UZa), olivine (UZb) and apatite (UZc) (Fig. 2). The relative thicknesses of these subzones, applied to the eastern, northern and western limbs, are listed in Table 1, which shows that UZa in the western limb, as measured in the Bierkraal drill core, is relatively thin (200 m). UZb is 400–700 m thick in all three limbs. In contrast, UZc is well over 1100 m thick in the western limb, considerably thicker than in the eastern and northern limbs. In contrast, MZ_U is 270 m thick in the western limb, but significantly thinner than in the east and north (Table 1, Fig. 2). Even this scheme is not perfect, as both olivine and apatite appear intermittently above their first appearance. Their absence in several intervals within UZb and UZc, and marked reversals in mineral compositions (see below) indicate that further subdivision is

Table 1: Stratigraphic thicknesses of subzones in the Main and Upper Zones of the Bushveld Complex

Subzone	Thickness (m)			
	West (1)	East (2)	East (3)	North (4)
Upper Zone c (UZc)	1128	910	350	610
Upper Zone b (UZb)	534	740	520	390
Upper Zone a (UZa)	200	580	640	590
Main Zone, upper portion (MZ_U)	273	700	590	—
Total stratigraphic thickness	2135	2930	2100	1590

(1) Bierkraal drill core, this study; (2) von Gruenewaldt (1973); (3) Molyneux (1974); (4) Ashwal *et al*. (2005).

required. Such subdivision has little application in the field, but is of great petrological significance. We refer to these further subdivisions as cycles.

Petrography

The gabbronorites, magnetite gabbros and diorites of MZ_U and UZ in the eastern limb have been well described previously (Wager & Brown, 1968; Willemse, 1969*a*; von Gruenewaldt, 1973; Molyneux, 1974), and only some important features are emphasized here, as the rocks of the western limb are extremely similar. Layering is intermittently present throughout the UZ. The magnetitite and nelsonite (magnetite–ilmenite–apatite Cumulate) layers are the most conspicuous (Fig. 3f); anorthosite layers are common and melanocratic facies occur less frequently. Any of the following minerals can occur as cumulus phases: plagioclase, olivine, clinopyroxene, orthopyroxene (and inverted pigeonite), magnetite, ilmenite, sulphides and apatite. Minerals that are only intercumulus are biotite, hornblende, quartz and potassium feldspar, and appear more abundantly toward the top of UZ. Alteration is only locally developed, and there has been no pervasive metamorphism.

The location of magnetitite and nelsonite layers in the Bierkraal core is shown in Fig. 2 and listed in Table 2. Gradations exist from almost magnetite-free anorthosites to magnetitite layers with over 95% oxide. Only those layers with greater than ~50% oxides and thicker than 2 cm are recorded in Fig. 2. There are 26 magnetitite and six nelsonite layers with a cumulative thickness of 20·4 m (Table 2). Their mineralogy and textures have been documented by Willemse (1969*b*), Reynolds (1985*a*), von Gruenewaldt *et al.* (1985), and von Gruenewaldt (1993). Footwall and hanging-wall rocks to magnetitite layers are commonly anorthositic, and lower contacts tend to be sharp, whereas upper contacts are gradational (von Gruenewaldt, 1973; Molyneux, 1974) (Fig. 3f). Anorthosites and, less commonly, other plagioclase-rich rocks, sometimes display a variably developed planar fabric, parallel to the layering (Figs 3a and b). Modal layering is occasionally developed in the interstitial phases to cumulus plagioclase (Fig. 3b). Plagioclase usually has euhedral to subhedral grain shapes, whereas olivine is anhedral even when it is abundant (Fig. 3d). Pyroxenes vary in shape (Fig. 3c). They are usually subhedral to anhedral, even when relatively abundant. In the upper parts of the UZ, clinopyroxene commonly displays ilmenite exsolution, and so TiO_2 and FeO(total) contents from electron microprobe analyses should not be considered primary. Apatite varies greatly in abundance, and always forms prismatic grains. They are commonly embedded in olivine- and magnetite-rich layers (Fig. 3d), but rarely in pyroxene and plagioclase. Magnetite is almost always anhedral. In the upper part of UZc, six nelsonite layers with up to 25% ilmenite and up to 30% apatite occur (Fig. 3e, Table 2) (Reynolds, 1985*a*; von Gruenewaldt, 1993), whereas below that level the magnetitite layers are devoid of apatite. Primary ilmenite is scarce in the lower half of UZ, but is ubiquitous as an exsolution phase.

Samples from the Bierkraal drill core

A subset of 55 samples from the Bierkraal drill cores was selected to obtain a systematic section of the MZ_U and UZ. These cores were previously investigated by Cawthorn & McCarthy (1985), Reynolds (1985*b*), Merkle & von Gruenewaldt (1986), Kruger *et al.* (1987), Cawthorn & Walsh (1988) and von Gruenewaldt (1993), but compositional data on the silicate minerals are few, apart from the interval across the Pyroxenite Marker (Cawthorn *et al.*, 1991). The Bierkraal core material, which was made available by the Geological Survey of South Africa, consists of three separate holes (BK1, BK2 and BK3) collared NE of Rustenberg in the western Bushveld Complex (Fig. 1). Correlation between the three cores has been presented (Walraven & Wolmarans, 1979; Kruger *et al.*, 1987), based on correlation of apatite- and magnetite-rich layers. The base of the Main Magnetitite Layer appears at depths of 171 m and 1378 m in BK2 and BK3, respectively (Kruger *et al.*, 1987, figure 2). In BK1 and BK3 the lowest occurrence of apatite–magnetite ferrodiorite cumulates is at ~1425 and ~375 m depth, respectively, and gives the best correlation. The composite section shown in Fig. 2 and used throughout this paper, is, therefore, composed of the interval from 415 m to 1600 m depth in BK1 at the top, followed by the interval from 550 m to 1420 m depth in BK3, and the interval from 200 m to 673 m depth in BK2 at the bottom. The true stratigraphic position is calculated assuming that

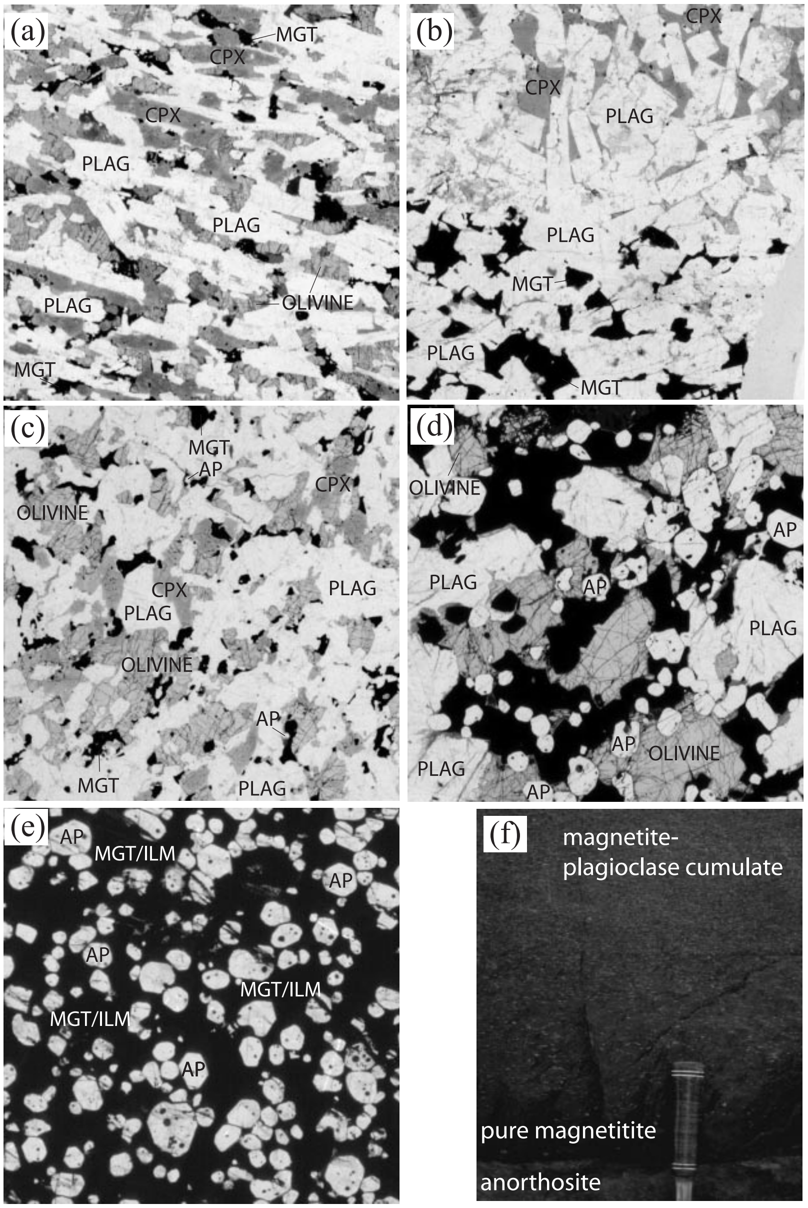

Fig. 3. Photographs showing typical textures of rocks from the Upper Zone of the Bushveld Complex. The field of view in all photomicrographs is 8 mm × 8 mm and all sections are cut vertically to the core, and so are nearly perpendicular to the layering. (a) Strong planar fabric, parallel to layering, displayed by cumulus plagioclase laths in UZc. Clinopyroxene, magnetite and olivine are anhedral, but their proportions suggest that they are cumulus phases. Sample 1w563.6. (b) Anorthosite in UZc. In the lower part the only poikilitic phase is magnetite, whereas in the upper part, it is exclusively clinopyroxene. Sample 1w1118.25. (c) Olivine–magnetite–apatite gabbro dominated by subhedral plagioclase and anhedral olivine, clinopyroxene and magnetite from UZc. Apatite is present, but rare in this photograph. Sample 1w1341.7. (d) Pods enriched in olivine, magnetite and apatite in a more leucocratic host dominated by plagioclase from UZc. Apatite is enclosed by olivine and magnetite, but seldom by plagioclase. Apatite is far less abundant in the plagioclase-rich areas. Sample 1w538.05. (e) Magnetite–ilmenite–apatite layer (nelsonite) from UZc. Apatite forms euhedral grains, whereas magnetite has polygonal grain boundaries. Sample 1w1111.5. (f) Field photograph of a magnetitite layer showing sharp contact to underlying anorthosite and up-section decreasing abundance of magnetite and increasing abundance of euhedral plagioclase laths. From Magnet Heights in the eastern limb. PLAG, plagioclase; CPX, clinopyroxene; MGT, magnetite; ILM, ilmenite; AP, apatite.

the core is vertical and igneous layering dips 24° north, and is reported in metres below the roof of the intrusion (located at 415 m depth in BK1). The investigated stratigraphic section between the Pyroxenite Marker and the roof is thus 2125 m thick, which is slightly greater than the standard section assumed for the western limb (2000 m; Eales & Cawthorn, 1996).

At the top of the ferrodiorite in BK1 is a quartzite fragment, interpreted to be a xenolith, and overlain by granophyric rocks. Both are intruded by granite sheets.

Table 2: Position and thickness of 26 magnetitite and six nelsonite layers, Bierkraal drill core, western Bushveld Complex*

Sample no.	Subzone	Stratigraphic position	Thickness (cm)
1w784†	UZc	337·1	2
1w823†	UZc	372·7	10
1w885†	UZc	429·3	6
1w1099†	UZc	624·8	10
1w1112.6†	UZc	637·3	30
1w1117	UZc	641·3	6
1w1206†	UZc	722·6	6
1w1284.1	UZc	793·9	3
1w1449.8	UZc	945·3	20
1w1450.5	UZc	945·9	10
1w1451.3	UZc	946·7	70
1w1460	UZc	954·0	710 (Layer 21)
1w1465	UZc	959·2	68
1w1485	UZc	977·4	25
1w1488.2	UZc	980·4	40
1w1489.2	UZc	981·3	3
1w1492.1	UZc	983·9	5
1w1492.65	UZc	984·4	20
1w1494	UZc	985·7	60
1w1532	UZc	1020·4	14
3w746	UZb	1261·5	80
3w927	UZb	1426·9	43
3w932	UZb	1431·5	60
3w942	UZb	1440·6	10
3w1247	UZa	1719·2	26
3w1272	UZa	1742·0	134
3w1294	UZa	1762·1	107
3w1313	UZa	1779·5	64
3w1315	UZa	1781·3	26
3w1343	UZa	1806·9	53
3w1368	UZa	1829·7	75
3w1378	UZa	1838·9	246 (MML)
Total thickness			2042

*Layers thicker than 2 cm.
†Nelsonite layers.
MML, Main Magnetitite Layer.

The granophyric rocks are interpreted to be the original roof rocks to the mafic sequence (Walraven, 1987). The presence of this complex succession intersected here means that it is not absolutely certain that the extreme differentiates of the mafic rocks have been preserved in this borehole. However, the iron-rich nature of the mafic minerals (see below) suggests that not much can be missing.

Analytical methods

Mineral compositions were obtained using a JEOL 8600 electron microprobe at the University of Aarhus, following the procedures described by Tegner *et al.* (1999). Plagioclase was analysed using a slightly defocused electron beam with a diameter of ~10 μm to minimize the effect of Na and K volatilization. Pyroxene and olivine were analysed using a focused electron beam with a diameter of ~2 μm to avoid problems of including inclusions and exsolution lamellae. Analyses of pyroxene, therefore, represent subsolidus equilibrium compositions. When possible, three points were analysed in the cores of each of three grains per sample, and the reported values (Table 3) are the average. Analyses of anhydrous minerals with either compositional anomalies indicating that impurities were analysed, or with an oxide sum lower than 98·5 wt % or higher than 101·5 wt % were excluded from the average values reported in Table 3. The full datasets for plagioclase, clinopyroxene, olivine and orthopyroxene are provided as Supplementary Datasets 1–4 (available at http://www.petrology.oupjournals.org).

Mineral separates of magnetite were prepared as described by Cawthorn & McCarthy (1980), and analysed for vanadium by X-ray fluorescence on pressed pellets. Standard SARM12 was used as reference and standard SARM38 for spiking of samples for calibration. Whole-rock powders were analysed for phosphorus also by X-ray fluorescence on pressed pellets, and published previously by Cawthorn & Walsh (1988).

Sr isotope compositions, and Sr and Rb concentrations (by isotope dilution) were analysed on whole-rocks by thermal ionization mass spectrometry (TIMS) at the Hugh Allsopp Laboratory of the Economic Geology Research Institute, University of the Witwatersrand, South Africa, following the procedure described by Eales *et al.* (1990). The whole-rocks were crushed in a jaw crusher, milled using a Siebtechnik swing mill, and finely ground in an automatic agate mortar and pestle. For dissolution, 0·1g aliquots of the powder were added to a previously spiked (^{84}Sr and ^{87}Rb) solution and dried in a Teflon beaker, and the mixture was dissolved in a mixture of distilled HF and HNO_3. The solutions were dried and taken up in 6N HCl, and checked for any residue. The solution was then dried and taken up in 2 ml 2·5N HCl and loaded on an ion exchange column and eluted and the Sr was recovered. A small proportion of the dried Sr was loaded with phosphoric acid on a single outgassed Ta filament and determined by TIMS using a multicollector system. The data reduction was done during the run. Rb was loaded on a double filament directly from the dissolved sample without separation from the matrix. Run temperature was controlled below the Sr evaporation of the side filament and

Table 3: Average mineral compositions, Bierkraal drill cores, western Bushveld Complex

Sample	Strat.	Zone	Cycle	Plagioclase		Clinopyroxene		Olivine		Orthopyroxene		Bulk-rock
no.*	pos.			An% (1 S.D.)	*n*	Mg# (1 S.D.)	*n*	Fo% (1 S.D.)	*n*	Mg# (1 S.D.)	*n*	Sr_0 (2 S.E.)
1w422.2	6·6	UZc	IX	43·0 (2·3)	9	11·4 (0·7)	6	3·0 (0·2)	6			
1w431.8	15·4	UZc	IX	45·2 (2·4)	9							
1w446.6	28·9	UZc	IX	42·8 (1·4)	9	4·9 (0·4)	7	1·3 (0·1)	9			
1w475.1	54·9	UZc	IX	43·4 (2·4)	8							
1w504.7	81·9	UZc	IX	45·1 (1·8)	9	15·9 (0·3)	6	3·9 (0·3)	9			
1w534	108·7	UZc	IX	44·6 (2·3)	8	30·8 (0·3)	4	9·4 (0·3)	9			
1w568	139·8	UZc	IX	50·0 (1·9)	9	36·4 (0·7)	4	10·4 (0·9)	9			
1w598	167·2	UZc	IX	46·3 (0·6)	8	26·8 (0·7)	7	7·8 (0·3)	9			
1w625.85	192·6	UZc	IX	49·8 (2·0)	8	50·2 (0·5)	3	21·4 (0·1)	9	36·9 (0·8)	6	
1w663.3	226·8	UZc	IX	48·7 (1·6)	9							
1w732	289·6	UZc	VIII	51·9 (0·8)	9	43·6 (1·0)	5	22·0 (0·2)	8			
1w770	324·3	UZc	VIII	49·3 (0·4)	9	46·9 (1·0)	4	21·6 (0·3)	9			
1w808.6	359·6	UZc	VII	50·5 (1·4)	8							
1w853.2	400·3	UZc	VII	49·8 (0·5)	8	46·2 (0·5)	6	18·7 (0·4)	9			
1w908.6	450·9	UZc	VII	49·5 (1·1)	8			13·3 (0·1)	4			
1w954	492·4	UZc	VI	49·8 (0·8)	8	35·7 (0·5)	6	14·8 (0·5)	9			
1w1010.2	543·7	UZc	VI	48·9 (1·3)	7							
1w1050.5	580·5	UZc	VI	50·1 (0·5)	8	36·2 (0·8)	5	15·9 (0·1)	9			
1w1138.2	660·5	UZc	VI	50·1 (0·9)	9	43·0 (0·4)	6	17·5 (0·4)	6			0·70711 (13)
1w1158.6	679·3	UZc	VI	48·1 (1·2)	6	25·5 (1·0)	5	6·2 (0·2)	9			0·70739 (14)
1w1190.1	708·5	UZc	V	45·6 (1·0)	7	32·5 (0·5)	6	14·6 (0·2)	9			0·70720 (13)
1w1239.5	752·8	UZc	V	48·3 (0·6)	9	38·3 (0·8)	5	16·0 (0·3)	8			0·70717 (15)
1w1303.2	811·2	UZc	V									0·70726 (13)
1w1329.2	835·1	UZc	V	50·9 (0·7)	8	47·3 (0·4)	4	23·2 (0·2)	9			0·70714 (13)
1w1423.4	921·2	UZc	V	52·0 (0·4)	9							
1w1488.85	981·0	UZc	V	55·0 (0·7)	9	57·8	1			44·9 (0·6)	15	0·70758 (16)
1w1507.0	997·5	UZc	IV	49·2 (0·8)	7	47·5 (1·3)	4			34·1 (0·7)	8	
1w1550.7	1037·5	UZc	IV	48·5 (0·9)	9	56·6 (0·7)	5	34·0 (0·2)	6			0·70726 (13)
3w540	1073·4	UZb	IV	49·8 (0·9)	8			37·5 (0·7)	9			
3w590	1119·0	UZb	IV	53·5 (1·3)	7							
3w640.9	1165·5	UZb	IV	55·9 (1·0)	9	61·7 (0·5)	6			50·4 (1·2)	6	
3w715	1233·2	UZb	III	52·1 (1·5)	9	64·3 (1·1)	8	38·9 (1·4)	9			
3w742	1257·9	UZb	III	55·4 (0·8)	9							
3w780	1292·6	UZb	III	57·7 (1·8)	9	59·6 (0·8)	9					
3w810	1320·0	UZb	III	58·2 (0·4)	8							
3w885	1388·5	UZb	II	56·4 (0·8)	9	59·7 (0·8)	5					
3w938	1436·9	UZb	II	57·8 (0·6)	8							
3w1015	1507·3	UZb	II	55·8 (0·7)	9							
3w1112	1595·9	UZb	II	56·3 (0·6)	8	64·1 (0·9)	8	44·2 (0·2)	3	56·1 (0·7)	6	
3w1212.25	1687·5	UZa	II	57·4 (0·8)	8							
3w1267.8	1738·2	UZa	II	58·5 (1·1)	9							
3w1268.9	1739·2	UZa	II	60·7 (0·7)	8	67·3 (1·1)	9					
3w1295	1763·1	UZa	II	59·9 (1·2)	9							
3w1314.7	1781·1	UZa	I	57·1 (0·9)	8	66·2 (0·7)	5			55·2 (0·5)	12	
2w124	1795·9	UZa	I	58·5 (0·5)	9							
3w1360	1822·4	UZa	I	61·1 (0·4)	9							
3w1381.25	1841·8	MZ_U	I	60·7 (0·8)	7	61·6 (3·4)	5			54·8 (0·1)	3	
2w225	1888·2	MZ_U	I	64·2 (0·6)	9							
2w324	1978·6	MZ_U	I	67·4 (1·4)	9	72·7 (1·5)	9			65·9 (0·5)	9	
2w402	2049·9	MZ_U	I	71·3 (2·0)	8	70·6 (1·0)	7			64·7 (0·3)	8	
2w448	2091·9	MZ_U	I	70·8 (2·8)	7							
2w481.9	2122·9	MZ_U	I	72·0 (2·4)	9	74·0 (0·8)	7			67·6 (0·4)	9	
2w491.9	2132·0	MZ_U		72·3 (1·0)	9							
2w601	2231·7	MZ_L		67·4 (0·4)	8							
2w672.8	2297·3	MZ_L		57·1 (1·3)	8							

An% = 100Ca/(Ca + Na); Mg# and Fo = 100Mg/(Mg + Fe); all molar proportions with all iron calculated as Fe^{2+}.
*Samples from drill core BK1 = 1w; BK2 = 2w; BK3 = 3w; for example, sample 2w402 is collected at 402 m depth in BK2.

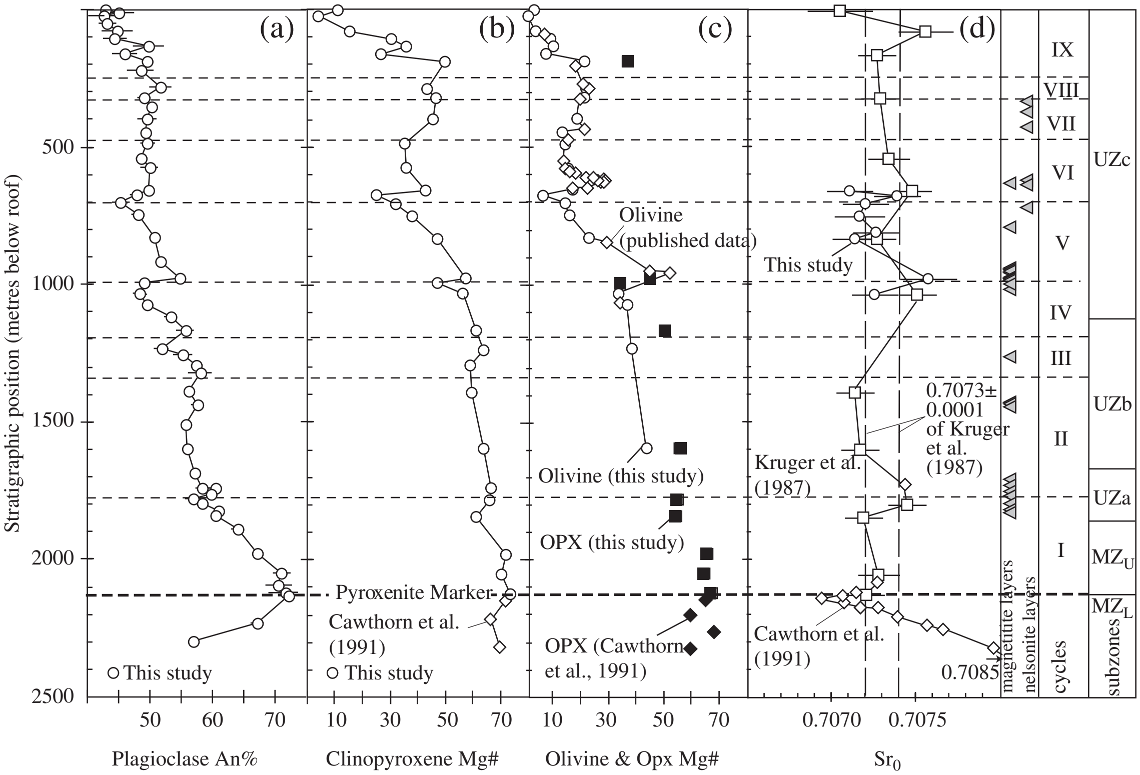

Fig. 4. Compositional variation of (a) plagioclase (An%), (b) clinopyroxene (Mg#), (c) olivine (Fo%) and orthopyroxene (Mg#) and (d) initial $^{87}Sr/^{86}Sr$ (Sr_0) with stratigraphic position in the Bierkraal drill cores. Data from Table 3, Supplementary Datasets 1–6, Reynolds (1985*b*), Merkle & von Gruenewaldt (1986), Kruger *et al.* (1987) and Cawthorn *et al.* (1991).

the ^{88}Sr peak position was monitored during the TIMS run. No Sr was detected in any run. The measured $^{87}Sr/^{86}Sr$ and the 2 S.E. (<0·011%) based on the run statistics are listed in Supplementary Dataset 5 (http://www.petrology.oupjournals.org). The accuracy of the measurements was determined by measuring the Eimar & Amend Sr standard, which gave $^{87}Sr/^{86}Sr$ of 0·70800 ± 0·00002 (2 S.E.), and the SRM987 standard, which gave $^{87}Sr/^{86}Sr$ 0·71023 ± 0·00002 (2. S.E.); these values are within error of the recommended values. Initial $^{87}Sr/^{86}Sr$ values, referred to as Sr_0, are calculated and reported in Table 3 and Supplementary Dataset 5. The 2 S.E. on Sr_0 is important to judge the petrogenetic significance of the measured $^{87}Sr/^{86}Sr$ and has been estimated using 14 replicates of a finely ground Bushveld norite. These replicates suggest that the 2 S.E. on measured $^{87}Sr/^{86}Sr$ is 0·018%. The 2 S.E. on $^{87}Rb/^{86}Sr$ used for age correction is considerably larger (1%) and depends on three factors: sample and spike weights and calibration errors in the spikes; sample heterogeneity; and analytical error. The total procedural blank values, which were determined to be <100 pg for both Rb and Sr, are ≪1% of the total sample and were ignored.

Mineral compositions and stratigraphic systematics

In the Bierkraal drill core, the compositions of plagioclase cores decrease systematically from An_{72} [$An = 100Ca/(Ca + Na)$] at the Pyroxenite Marker to An_{43} at the top of UZc (Fig. 4a). This up-section decline, however, is not continuous as assumed in previous studies based on few and widely spaced samples (Wager & Brown, 1968; von Gruenewaldt, 1973; Molyneux, 1974). Several up-section increases in An% are significantly larger than analytical error (±1 S.D.) and are not artefacts of correlation between the three cores sampled (Table 3). We refer to these stratigraphic intervals as reversals. The sections between reversals display either near-constant or up-section declining An% (Fig. 4a). We have used the reversals to higher An% as one criterion to subdivide MZ_U and UZ into cycles that are unrelated to the accepted zonal subdivision (Figs 2 and 4). The reversals typically occur over 15–175 m of section and range in magnitude from 3 to 6 An% (Table 3, Fig. 4a). For comparison, plagioclase changes from An_{57} to An_{72} over ∼180 m section in the reversal across the Pyroxenite Marker (Fig. 4a) (Cawthorn *et al.*, 1991). Given the average spacing of ∼40 m between samples, the exact location of cycle boundaries is only approximate. For the section from the Pyroxenite Marker to the middle of UZc, we have chosen to place the base of each cycle immediately below the lowest sample showing a marked reversal in An%. In this way, we have identified cycles I–VI (Fig. 4a; Table 3). In Fig. 4, a further three cycles (VII–IX) are shown where there is no apparent reversal in An%. These cycles are defined on the basis of the disappearance of apatite, but can be explained in the same way as cycles I–VI (see discussion). Within some cycles (I, IV, and V), An% declines smoothly up-section, with an average rate of decline of one An% per 18–27 m of section. In other cycles (II, VI–VIII), the trends are largely dispersed around a constant An% (Fig. 4a).

The Mg# [100Mg/(Mg + Fe)] of clinopyroxene declines from 74 at the Pyroxenite Marker to Mg#$_{cpx}$ 5 close to the top of the core (Fig. 4b, Table 3) and correlates positively with An% (Fig. 5). As with plagioclase, clinopyroxene displays reversals in Mg#$_{cpx}$ across several cycle boundaries. The most marked reversals in Mg# are between cycles IV and V (48–58) and between V and VI (26–43). In cycles VI–VIII, the sample spacing is too large to resolve reversals in Mg#$_{cpx}$, but a general up-section increase from 43 to 50 is evident. In the middle and upper portion of cycle IX, Mg#$_{cpx}$ drops rapidly from 50 to 5 close to the top. Similar to the section across the Pyroxenite Marker (Cawthorn *et al.*, 1991), the stratigraphic position of reversals in An% and Mg# may be slightly offset (Fig. 4b; Table 3). The rate of upward decline in Mg#$_{cpx}$ is moderate in the lower cycles I and II at one Mg# unit per ~24 and ~74 m of section, respectively. In cycles IV and V, the rate of decline is greater at 1 Mg#$_{cpx}$ per ~11 and 9 m, respectively. An important observation for the following discussion of the differentiation trend is that cumulate rocks with Mg#$_{cpx}$ and plagioclase An% >52, Mg#$_{cpx}$ is larger than An% whereas the reverse pattern is observed in the more evolved cumulates (Fig. 5).

The up-section variation in the Fo content [100Mg/(Mg + Fe)] of olivine (Fig. 4c) is shown not only by our new data (22 samples; Table 3) but also previously published electron microprobe data for BK1 by Reynolds (1985*b*; eight samples), Merkle & von Gruenewaldt (1986; nine samples) and unpublished data (seven samples) from 1980 by R.G.C., obtained using the electron microprobe at the University of Bloemfontein, South Africa (Supplementary Dataset 6; http://www.petrology.oupjournals.org). The Fo% decreases from Fo$_{44}$ in cycle II to Fo$_1$ at the top of UZc. Again, this up-section decrease in Fo content is interupted by reversals that coincide with reversals in Mg#$_{cpx}$ and An% (Fig. 4). Some of these increases in Fo% are relatively large, for example from Fo$_{34}$ to Fo$_{52}$ across the boundary between cycles IV and V and from Fo$_6$ to Fo$_{29}$ between cycles V and VI. Within cycle V, the olivine composition changes from Fo$_{54}$ to Fo$_6$ over only 300 m of stratigraphic section. As observed for the Mg#$_{cpx}$ and An% from the top of cycle VI to the base of cycle IX, the Fo% is dispersed around a slightly increasing trend. Above this level, Fo% declines sharply to virtually pure fayalitic compositions at the top of UZc. Figure 4c also shows that the Mg# of orthopyroxene in 10 samples ranges from Mg#$_{opx}$ 68 to Mg#$_{opx}$ 34. Although the samples are widely spaced, Mg#$_{opx}$ conforms with the trends shown by Mg#$_{cpx}$ and Fo%. The Fe/Mg exchange coefficient K_D(Fe/Mg) between orthopyroxene and clinopyroxene is relatively constant (1·3 and 1·4; five pairs) in cycle I, but increases to 1·7 (three pairs) in cycle IV. This is similar to experimental data for Fe/Mg exchange between coexisting pyroxenes (Toplis & Carroll, 1995), suggesting that the pyroxenes are in equilibrium.

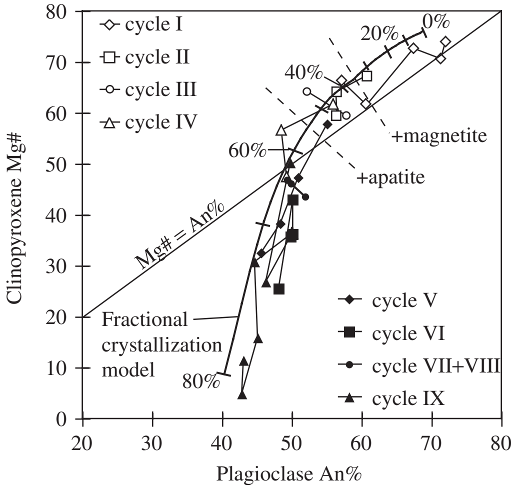

Fig. 5. Mg# of clinopyroxene vs An% of plagioclase for the nine cycles in MZ$_U$ and UZ of the Bierkraal drill cores. Data from Table 3. Continuous line with tick marks shows calculated Mg# of clinopyroxene and An% of plagioclase for a forward fractionation model. Data from Table 5. Tick marks each represent 10% crystallization. Dashed lines mark the approximate onset of magnetite and apatite crystallization. Fine continuous line shows Mg# = An%.

Plagioclase An% across magnetitite layers

In the Bierkraal drill core some of the reversals in plagioclase An% occur in sequences with abundant magnetitite layers, whereas others occur in normal leucocratic gabbronorites (Fig. 4). A detailed study of plagioclase composition across magnetitite layers in these cores is being undertaken, but here we refer to the relationship between An% across magnetitite layers (Fig. 6) in closely spaced gabbronorite samples across the Main Magnetitite layer and the two subsidiary magnetitite layers (Layer 1, Layer –3) below and above the Main Magnetitite Layer from outcrops at Magnet Heights in the eastern limb (Fox, 1982). Although the plagioclase

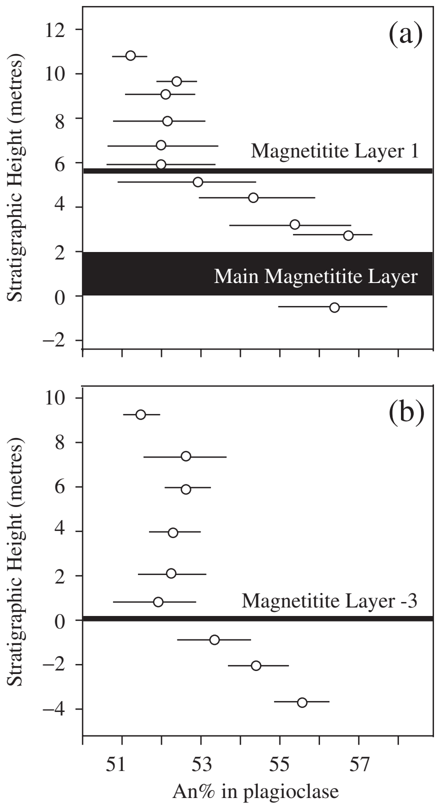

Fig. 6. Compositional data for plagioclase (An%) across (a) the Main Magnetitite Layer and Magnetitite Layer 1, and (b) Magnetitite Layer −3 at Magnet Heights in the eastern limb of the Bushveld Complex. Data from Fox (1982).

composition varies from An_{51} to An_{57} and displays a systematic up-section decrease below magnetitite layers 1 and −3, the An% is identical within error in samples immediately below and above each of the three magnetitite layers. Similarly, Harney *et al.* (1996) found no change in the An content of plagioclase below and above two sections of the Main Magnetitite Layer. These data suggest that fluctuations in An content are not specifically related to the formation of magnetitite layers.

V_2O_5 content of magnetite

The V_2O_5 content of magnetite, separated from 266 samples, is shown in Fig. 7. From its first appearance as a cumulus mineral near the top of cycle I to the base of cycle IV the concentration decreases relatively uniformly from about 1·7 to 0·4% (excluding two aberrant values in cycle III). Through the remainder of cycle IV, and in each of the subsequent cycles it shows relatively high concentrations near the bases and rapid decreases up-section, reaching close to detection limits near the top of each cycle. However, the highest concentrations do not occur abruptly at the bases of each cycle, but climb from the low values from the top of the previous cycle to a high value typically several tens of metres above the reversal identified by the plagioclase composition. Thus, there is no close relation between the presence of magnetitite layers and reversals in V content.

Sr isotope compositions

The initial $^{87}Sr/^{86}Sr$ (Sr_0) composition of the Bierkraal drill cores was determined previously and showed a marked shift across the Pyroxenite Marker from ~0·7085 in MZ_L to ~0·7073 in MZ_U and UZ (Kruger *et al.*, 1987; Cawthorn *et al.*, 1991) (Fig. 4). The constancy of Sr_0 above the Pyroxenite Marker, determined as 0·7073 ± 0·0001 (2 S.E.) from the intercept of a 2066 ± 58 Ma regression line in an isochron diagram (Kruger *et al.*, 1987), was explained by complete mixing and homogenization between residual ($Sr_0 = 0{\cdot}7085$) and recharged ($Sr_0 = 0{\cdot}7067$) magma in proportions close to 1:1. The near-constancy of Sr_0 also implies that addition of further magma above the Pyroxenite Marker can be ruled out, unless it had Sr_0 of ~0·7073 (Kruger *et al.*, 1987; Cawthorn *et al.*, 1991). Because our interpretation of the cycles presented here hinges on whether new magma was added or not, we have determined Sr isotope compositions for eight additional samples across the boundaries between cycles IV, V and VI. Seven of the eight new Sr_0 determinations range from 0·7071 to 0·7074 (Fig. 4; Table 3) and are within error of 0·7073 ± 0·0001 determined previously for MZ_U and UZ (Kruger *et al.*, 1987). Although the Sr_0 (0·7076 ± 0·0002) of sample 1w1488.85 (stratigraphic height of 980 m) at the base of cycle V is marginally higher than that of the other samples analysed (Table 3, Fig. 4), the combined Sr isotope datasets suggest constancy of Sr_0 in MZ_U and UZ. The Sr_0 of proposed recharge magmas to the entire Bushveld Complex ranges from 0·7045 to 0·7090 but none has compositions close to 0·7073 (Kruger, 1994). In the Bethal area located SW of the eastern limb (Fig. 1), subsurface mafic rocks have Sr_0 of 0·7055 and have been explained as the products of crystallization from unadulterated Upper Zone magma (Kruger, 2005). We therefore conclude that recharge with magma with Sr-isotopic composition similar to proposed Bushveld magmas can be ruled out. Therefore, an internal mechanism for generation of the layered MZ_U and UZ sequence must be sought.

Phosphorus content in whole-rock samples

Figure 7a shows the variation in bulk-rock P_2O_5 (wt %) of the Bierkraal drill cores [data from Cawthorn & Walsh (1988)]. In the lower part from cycle I to the basal part of cycle IV, apatite is not a cumulus phase and P_2O_5 is very low (<0·10 wt %). In the middle and upper

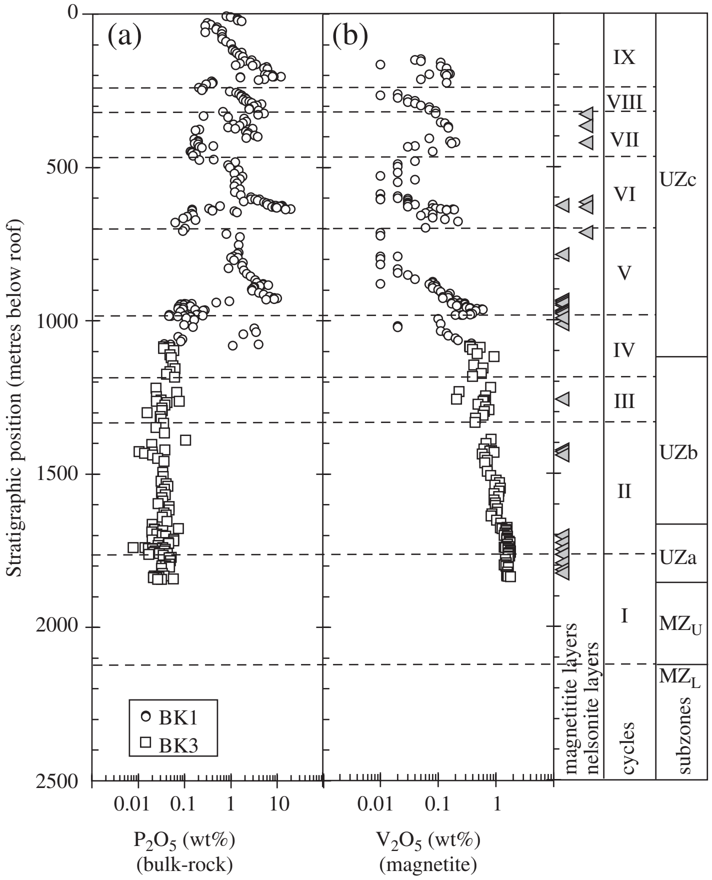

Fig. 7. Wt % P_2O_5 (a) of whole-rocks and V_2O_5 in magnetite (b) plotted against stratigraphic position in the composite section based on the Bierkraal drill cores. (Note logarithmic scales on the *x*-axes.) Phosphorus data from Cawthorn & Walsh (1988); V data are given in Supplementary Dataset 7.

part of cycle IV, P_2O_5 is highly variable and a number of samples contain between 1 and 10 wt % (Fig. 7a). Abundant cumulus apatite at this level is taken as defining the base of UZc, as discussed above. Above this level, P_2O_5 displays pronounced cyclicity. In cycle V, P_2O_5 is low (<0·3 wt %) in the basal 50 m, but increases up-section to 9·9 wt % over only 16 m (Fig. 7a; Supplementary Dataset 7, available at http://www.petrology.oupjournals.org). Hereafter, P_2O_5 declines smoothly to 0·8 wt % through 210 m of section. In the following 56 m, P_2O_5 drops to much lower values (0·09–0·17 wt %) and apatite is no longer a cumulus phase. The subsequent low-P interval (50 m thick, and defined by seven samples) coincides with the reversal in An%, Mg#$_{cpx}$ and Fo% between cycles V and VI (Fig. 4). A similar pattern in P_2O_5 is repeated four times in the upper portion of the core (Fig. 7a). For reasons discussed below, we have placed a cycle boundary at the base of each low-P_2O_5 interval as shown in Figs 4 and 7. In cycle VI, the most apatite-rich rocks are nelsonite layers (Fig. 3e), which exhibit extremely high contents of up to 19·5 wt % P_2O_5 (Fig. 7a; Supplementary Dataset 7). The associated normal leuco- and mesocratic ferrodiorite samples contain up to 10 wt % P_2O_5 (Cawthorn & Walsh, 1988). Another observation is that the P_2O_5 content of low-P_2O_5 intervals increases gradually up-section from <0·1 wt % below the appearance of apatite to ~0·4 wt % at the top of the core (Fig. 7a). A total of 450 analyses of P_2O_5 were obtained through the Upper Zone (Cawthorn & Walsh, 1988), and so the location of breaks is more rigorously defined than by other criteria.

FRACTIONATION MODELLING

Background and assumptions

To guide the quantitative interpretation of the evolution of the entire Main–Upper Zone succession, and the differentiation in each cycle as shown by mineral compositions (Figs 4 and 7b) and bulk-rock P_2O_5 contents (Fig. 7a), we have estimated the possible compositions of evolving residual magma and equilibrium cumulate

Table 4: Calculation of parent magma composition at the level of the Pyroxenite Marker

Oxide (wt %)	Average composition of cumulate above Pyroxenite Marker 1	Estimate of residual melt at Skaergaard 2	Quenched melt, A 3	Quenched melt, B 4	Quenched melt, C 5	Calculated composition of melt at Pyroxenite Marker 6
SiO_2	47·6	73·2	64·3	66·1	66·6	51·4
TiO_2	1·2	0·5	2·0	2·1	0·4	1·0
Al_2O_3	17·3	13·3	12·0	13·4	13·6	16·6
FeO(total)	13·5	3·8	9·6	5·8	4·6	11·7
MnO	0·2		0·1			0·1
MgO	5·6	0·2	1·2	1·6	0·5	4·6
CaO	11·0	1·8	4·3	3·7	4·5	9·7
Na_2O	2·7	4·1	3·6	2·3	3·9	2·9
K_2O	0·4	3·3	1·8	2·9	1·8	0·7
P_2O_5	0·44			1·1	0·1	0·4
Total	99·9	100·2	98·8	99·0	96·0	99·1

Column 1: average of all compositions (44 samples) of rocks above the level of the Pyroxenite Marker in the eastern Bushveld given by von Gruenewaldt (1971) plus 1 wt % titanomagnetite. Column 2: estimate of residual melt after 75% crystallization of the Skaergaard intrusion (Hunter & Sparks, 1987). Column 3: quenched melt analysed by Toplis & Carroll (1995) formed at 1057°C. Column 4: quenched melt analysed by vander Auwera & Longhi (1994) formed at 1071°C. Column 5: quenched melt analysed by Spulber & Rutherford (1983) formed at 927°C. No value for phosphorus was given. We have included 0·1% for the purpose of this calculation. Column 6: calculated melt compositon present at level of Pyroxenite Marker, assuming 80% cumulate (column 1) and 20% residual melt (column 5).

assemblage using a forward model of closed-system fractional crystallization of a plausible parental magma. Below, we first present the assumptions and rationale used in estimating the parental magma for the cumulate rocks above the Pyroxenite Marker. We then describe the mass-balance calculations for fractional crystallization. A simple mass-balance calculation is preferred because thermodynamic algorithms simulating crystallization (e.g. Ariskin *et al.*, 1993; Ghiorso & Sack, 1995) cannot be constrained for evolved, ferrodioritic magmas such as those appropriate to this section of the Bushveld Complex.

In applying such thermodynamic algorithms, specific problems arise with selection of fO_2 and H_2O content. The water content of basic magmas is probably low. However, because calculations of up to 80% fractionation are considered here, the water content and its partial pressure may become significant, as demonstrated by the presence of hornblende (although not as a cumulus phase) in the evolved Bushveld rocks. The stability of magnetite and its proportion crystallizing is very strongly influenced by fO_2. In the experimental study by Toplis & Carroll (1995), they presented analyses of two quenched liquids formed at the same temperature (1072°C) from the same starting composition, but at fO_2 differing by 2 log units that contained 62 and 53 wt % SiO_2 and 9 and 17 wt % FeO (total), respectively. In fact, much of the debate about the evolution of the Skaergaard intrusion hinges around this issue [see summary by Tegner (1997)]. In the Upper Zone of the Bushveld Complex, there is no independent measure of the prevailing fO_2 or whether it remained constant. Thus, calculations that require knowledge of fO_2 are not constrainable, and we prefer to use a mass-balance approach that includes the mineral proportions actually observed in the succession.

Calculated parental magma composition

The preferred, calculated parental magma composition that produced the succession from the Pyroxenite Marker to the top of the intrusion is given in column 6 of Table 4. To obtain this estimate we have determined the bulk composition of the preserved cumulates and added an estimated evolved residual component that is thought to have escaped from the intrusion (Cawthorn & Walraven, 1998). Outcrop of the western limb of the Bushveld Complex is poor, and most studies on the Main and Upper Zones have been undertaken on the eastern limb. Specifically, we note that no systematic study of whole-rock compositions is available from the western limb. However, there are remarkable similarities of the entire sequence and also distinctive layers in both limbs, such as the Pyroxenite Marker, the Main Magnetitite Layer (~2 m thick) and Magnetitite Layer 21 (~7 m thick), and also identical initial Sr isotope ratio

(Eales & Cawthorn, 1996). Hence, in the absence of suitable data from the western limb, we resort to information and data from the eastern limb in the following discussion. We have averaged all the whole-rock analyses from von Gruenewaldt (1971) for this section in the eastern limb. No analyses of magnetitite layers were included. Our measurements here (Table 2) suggest that the magnetitite layers comprise 20 m out of 2125 m, or 1% of the total thickness. Hence, we have added the equivalent of 1% titanomagnetite to this average. This bulk composition is given in Table 4, column 1. The CIPW norm of this composition contains 15% olivine, 15% diopside and 5% hypersthene. Such a melt composition, if totally liquid, would crystallize olivine, and so is not consistent with the observed gabbronoritic mineral assemblages in the MZ_U.

Cawthorn & Walraven (1998) used a mass-balance approach involving the compilation of minor and trace element data for this entire section to suggest that there had been loss of some evolved magma during crystallization. The composition and proportion of this lost component is impossible to quantify from the Bushveld rocks themselves. The most evolved rocks found in the intrusion are almost certainly cumulative and so do not represent melt compositions. This final melt must have been in equilibrium with olivine, orthopyroxene, clinopyroxene, plagioclase, magnetite, ilmenite and apatite. We have not found any experimental data that perfectly fit this requirement, but present some analyses in Table 4 that probably bracket this composition. Vander Auwera & Longhi (1994) gave an analysis of a melt in equilibrium with orthopyroxene, pigeonite, plagioclase, clinopyroxene, ilmenite and magnetite at 1071°C. Toplis & Carroll (1995) gave an analysis of melt in equilibrium with plagioclase, clinopyroxene, magnetite and ilmenite at 1057°C. Spulber & Rutherford (1983) gave an analysis of melt in equilibrium with olivine, clinopyroxene, pigeonite, plagioclase, ilmenite and magnetite at 925°C, which we consider to be a plausible temperature for the final residual melt for the Bushveld Complex. By way of comparison, we include in Table 4 a calculated composition for the evolved magma to the Skaergaard intrusion by Hunter & Sparks (1987). These analyses probably bracket the melt composition at the end of differentiation of the Upper Zone in the Bushveld Complex. The proportion of this melt that has escaped is even harder to predict, but Cawthorn & Walraven (1998) estimated 20%. We have added 20% of the analysis determined by Spulber & Rutherford (1983) to the bulk cumulate composition in Table 4 as an approximation to the melt that existed at the level of the Pyroxenite Marker. The CIPW norm of this composition contains 1% quartz, 13% diopside and 22% hypersthene, and is expected to crystallize orthopyroxene rather than olivine. We note that this estimate of melt composition is model-dependent, but we demonstrate that it yields an internally consistent fractionation model. Our physical model, presented below, does not depend upon the quantitative accuracy of this composition, but it provides an illustration of plausible differentiation trends.

Cumulus proportions and mineral compositions

The cumulus proportions, in weight per cent, have been calculated from the modal data of von Gruenewaldt (1971) for each subzone, and are given in Table 5 and Fig. 8. The differentiation of the proposed parental magma at the level of the Pyroxenite Marker (column 6 in Table 4) has been modelled in steps of 2% crystallization (Table 5; Fig. 8). Gabbronorite crystallizes to produce the MZ_U. Magnetite co-crystallization is assumed to begin at $Mg\#_{cpx}$ ~67 and An% ~61, as observed in this study (Fig. 4). This produces cumulate rocks with modes similar to those of UZa (Table 5; Fig. 8). Olivine is then assumed to co-precipitate to produce cumulate rocks similar to UZb. Apatite is assumed to join the crystallizing assemblage when the P_2O_5 content of the evolving magma reaches 1·0 wt % (Cawthorn & Walsh, 1988) to form cumulates equivalent to those of UZc.

The Mg# values of olivine, ortho- and clinopyroxene are calculated assuming a K_D(Fe/Mg) between crystal and melt that changes linearly from 0·3 to 0·4, 0·29 to 0·24 and 0·25 to 0·19, respectively, during crystallization (Toplis & Carroll, 1995; Toplis, 2005). Minor oxide abundances in calculated pyroxene compositions used in our calculations are intermediate between those of Atkins (1969), based on mineral separates, and our electron microprobe data. The former may include impurities, whereas the latter are influenced by exsolution effects. Al_2O_3 contents are 2 and 1 wt % for clinopyroxene and orthopyroxene. CaO is taken as occupying 0·9 cation positions in the clinopyroxene formula, and 2% in orthopyroxene. TiO_2 contents are calculated using a partition coefficient of 0·4 for clinopyroxene. For plagioclase, K_D(Na/Ca) is assumed to change from 0·8 to 1·4 during crystallization (Toplis & Carroll, 1995).

Ilmenite comprises less than 10% of the oxide phase through most of the Upper Zone, and becomes a significant cumulus phase only towards the extreme top of this section (Reynolds, 1985*b*). However, its modal proportion is not quantified, and so it has not been included in these models. It is qualitatively included in the calculations, in that the titanomagnetite composition that is extracted in these calculations increases from 10 to 20 wt % TiO_2 from bottom to top of the Upper Zone (Molyneux, 1972; Reynolds, 1985*b*).

Table 5: Calculated compositions of magma, cumulate, and minerals, and magma density, in fractional crystallization model

F:	1·00	0·90	0·80	0·70	0·64	0·54	0·46	0·30	0·20
Mineral appearing:	Pl,Op,Cp				Mgt	Ol	Ap		
Magma composition (wt %)									
SiO_2	51·40	52·09	52·16	52·24	52·29	53·33	54·66	60·44	67·72
TiO_2	1·00	1·12	1·24	1·41	1·53	1·42	1·31	0·93	0·57
Al_2O_3	16·60	16·53	16·20	15·82	15·55	15·09	14·66	13·50	12·10
Fe_2O_3	1·50	1·67	2·02	2·50	2·88	2·67	2·46	1·87	1·20
FeO	10·20	10·83	11·25	11·68	11·91	12·22	12·17	10·61	7·33
MgO	4·60	4·24	3·76	3·20	2·83	2·39	1·88	0·70	0·07
CaO	9·50	9·26	8·84	8·33	7·98	7·42	6·95	5·41	3·72
Na_2O	2·90	3·03	3·14	3·25	3·33	3·48	3·61	3·92	4·06
K_2O	0·70	0·77	0·86	0·96	1·04	1·21	1·40	2·10	3·08
P_2O_5	0·40	0·45	0·51	0·58	0·64	0·75	0·89	0·51	0·14
Magma density (g/cm^3)	2·68	2·68	2·69	2·69	2·70	2·68	2·66	2·57	2·45
Proportion of cumulus minerals									
Plagioclase	0·58	0·58	0·58	0·58	0·57	0·57	0·57	0·57	0·57
Orthopyroxene	0·17	0·17	0·17	0·17	0·12	0·07	0·05	0·05	0·05
Clinopyroxene	0·25	0·25	0·25	0·25	0·21	0·18	0·13	0·13	0·15
Olivine	0·00	0·00	0·00	0·00	0·00	0·08	0·13	0·13	0·13
Magnetite	0·00	0·00	0·00	0·00	0·10	0·10	0·10	0·08	0·08
Apatite	0·00	0·00	0·00	0·00	0·00	0·00	0·03	0·03	0·02
*Mineral compositions**									
Cpx Mg#	76·3	74·6	72·4	69·2	66·6	63·1	58·3	38·9	8·9
Opx Mg#	73·2	70·4	66·9	62·4	58·9	54·1	48·4	28·7	5·6
Ol Fo%						49·6	43·1	23·3	4·2
Plag An%	68·5	67·0	65·2	63·0	61·4	58·7	56·1	47·8	37·8
Cumulate bulk composition									
SiO_2	51·90	52·00	52·13	52·26	47·14	46·07	44·36	44·95	46·70
TiO_2	0·09	0·10	0·11	0·12	2·11	2·09	2·06	1·64	1·63
Al_2O_3	19·49	19·34	19·16	18·95	18·26	17·81	17·32	16·51	15·61
Fe_2O_3	0·00	0·00	0·00	0·00	5·50	5·50	5·50	4·40	4·40
FeO	5·20	5·64	6·17	6·89	8·17	10·28	12·06	14·45	18·13
MgO	8·57	8·25	7·88	7·37	5·39	5·53	4·95	2·78	0·56
CaO	12·99	12·80	12·57	12·29	11·20	10·29	10·36	9·12	7·99
Na_2O	2·07	2·17	2·29	2·44	2·50	2·69	2·85	3·41	4·09
K_2O	0·13	0·13	0·13	0·13	0·13	0·13	0·13	0·13	0·13
P_2O_5	0·00	0·00	0·00	0·00	0·00	0·00	1·68	1·40	1·12

Pl, plagioclase; Op, orthopyroxene; Cp, clinopyroxene; Mgt, magnetite; Ol, olivine; Ap, apatite. *F*, fraction of melt remaining.

*Calculated compositions of minerals extracted in the fractionation model are given in Supplementary Dataset 8.

Evolution of melt composition

Over the interval from 0 to 80% crystallization ($F = 1$–$0{\cdot}2$), the calculated residual magma evolves from a slightly iron-rich tholeiitic basalt (51·4 wt % SiO_2, 4·6 wt % MgO, 11·6 wt % FeO^{tot} and 3·6 wt % $Na_2O + K_2O$) to an iron-rich dacite with 67·7 wt % SiO_2, 0·1 wt % MgO, 8·4 wt % FeO^{tot} and 7·2 wt % $Na_2O + K_2O$ (Table 5). During crystallization of rocks corresponding to MZ_U, the forward model predicts that the FeO^{tot} of the magma increases to ~14·5 wt % and SiO_2 remains largely constant at ~52 wt % (Table 5, Fig. 8). In the crystallization interval where magnetite gabbronorites equivalent to UZa are produced, SiO_2 starts to increase slightly and FeO^{tot} remains constant.

(a) Mineral proportions assumed in cumulates

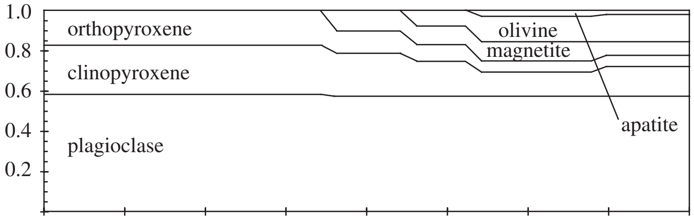

(b) Model magma composition (wt%)

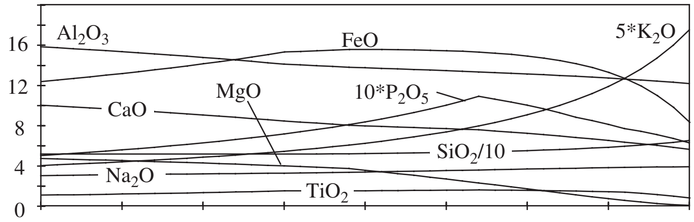

(c) Model plagioclase and augite composition in cumulates

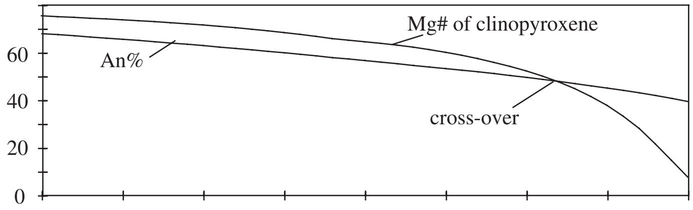

(d) Model magma density (g/cm^3)

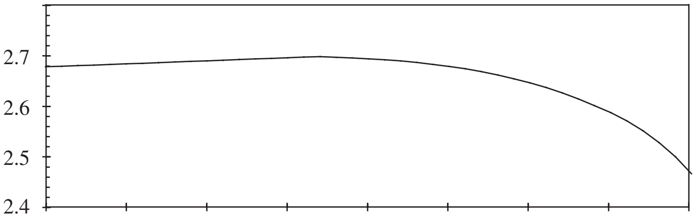

(e) Subzones in the Bushveld Complex corresponding to the model

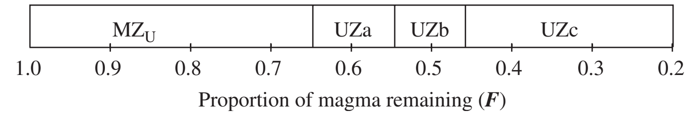

Fig. 8. Results of a forward, incremental fractional crystallization model. Data from Table 5 (see text for explanation). (a) Mineral proportions assumed in the extracted cumulate rock. (b) Major element liquid line of descent. (c) Calculated Mg# of clinopyroxene and An% of plagioclase in equilibrium with the magma. (d) Calculated magma density. (e) Subzones in the Bushveld Complex corresponding to the model.

In the crystallization interval corresponding to UZb, the appearance of iron-rich olivine in the crystallization assemblage causes an increase in melt SiO_2 to 55 wt %, and FeO slowly decreases. In the more evolved model magmas, crystallization of apatite–magnetite–ilmenite olivine gabbronorites equivalent to UZc drive SiO_2 up to 67·7 wt % and FeO down to 8·4 wt % after 80% crystallization.

Evolution of melt density

The density of the evolving magma is perhaps the most important factor in magma chamber dynamics and has been calculated following McBirney (1993), including the partial molar volume of phosphorus (Toplis *et al.*, 1994). During crystallization of rocks of the MZ_U, the calculated magma density increases from 2·68 to 2·70 g/cm^3 (Table 5, Fig. 8). After magnetite starts to crystallize at the level corresponding to the base of UZ, magma density decreases continuously and reaches 2·45 g/cm^3 after 80% crystallization.

Evolution of cumulus mineral compositions

Over the interval from 0 to 80% crystallization, Mg#$_{cpx}$ in equilibrium with the evolving magma decreases from 76 to 9 and the An% of equilibrium plagioclase changes from 69 to 38 (Fig. 8c, Table 4). The first olivine to crystallize is Fo$_{50}$ and after 80% crystallization it has evolved to Fo$_4$ (Table 5). The slow evolution of An% relative to Mg#$_{cpx}$ is explained by a modest K_D(Na/Ca) for plagioclase, close to unity (0·8–1·4), whereas the K_D(Fe/Mg) values for the mafic phases are lower (0·19–0·35) and produce more dramatic changes in Mg#. This results in a cross-over from cumulates where Mg#$_{cpx}$ exceeds An% in the interval from 0 to 65% crystallization, to the opposite in the more evolved magmas (Fig. 8c). In other words, the model predicts the typical fractionation trend of tholeiitic intrusions towards extremely iron-rich end-members of the mafic phases, whereas the An% of plagioclase remains relatively elevated, e.g. An$_{32}$ in the Skaergaard intrusion (Wager & Brown, 1968; Tegner, 1997) and An$_{30-40}$ in the Bushveld Complex (Wager & Brown, 1968; von Gruenewaldt, 1973; Molyneux, 1974; Ashwal *et al.*, 2005; this study) (Fig. 5).

DISCUSSION

Mineral compositions

We note a caution regarding comparison between calculated mineral compositions and electron microprobe analyses (Fig. 5). We have analysed the cumulus core of plagioclase grains. Even in zoned grains, diffusion will be extremely slow (Morse, 1984), and so primary compositions will be preserved. However, for the mafic minerals post-cumulus re-equilibration will occur, and zoned grains will homogenize. Furthermore, Mg and Fe partitioning between clinopyroxene and orthopyroxene changes with falling temperature, as first documented by Kretz (1963), and applied to the pyroxenes of the Bushveld Complex by Atkins (1969). We note variations in the K_D(Fe/Mg) values between the two pyroxenes in our data, which we attribute in part to the slow cooling of the intrusion. Also, the clinopyroxenes in the Upper Zone display exsolution of ilmenite, which will also cause a change in the Mg# of the electron microprobe analysis of clinopyroxenes relative to its primary composition. Also important is the effect of reaction with trapped liquid (Barnes, 1986). Such reaction will produce variable degrees of iron enrichment in the finally equilibrated pyroxenes (Lundgaard *et al.*, 2006). All of these processes will variably influence the analysed mafic mineral composition, and hence the analysed Mg# should not be considered as rigorous an indication of evolving melt composition as the An value of the plagioclase. Finally, when comparing observed Mg# with that calculated in the model it needs to be borne in mind that the effect of ferric iron has not been considered. The calculated composition, for example of clinopyroxene, uses the proportion of ferrous iron only. In contrast, the electron microprobe analysis includes ferric iron as well. The difference that this introduces can be demonstrated using a clinopyroxene analysis by Atkins (1969; his analysis 8) from the base of the UZ in which ferric iron has been determined. The Mg# value calculated using ferrous iron only gives 72·7, whereas if total iron is used the figure becomes 70·7. Hence, the calculated value (below) will always exceed that of the determination by electron microprobe.

Magma chamber dynamics

The up-section breaks between cycles to higher Mg# of pyroxene and olivine, higher An% of plagioclase and higher V_2O_5 of magnetite, and the intermittent disappearance of olivine and apatite (Figs 4 and 7) require a mechanism in addition to the simple, closed-system fractional crystallization model, often assumed for this section of the Bushveld Complex (Wager & Brown, 1968; von Gruenewaldt, 1973; Molyneux, 1974). In a detailed study of the Main and Upper Zones in the Bellevue drill core of the northern limb, Ashwal *et al.* (2005) explained reversals in An% of plagioclase and Mg# of pyroxene by magma recharge. However, as discussed above, the constancy of Sr$_0$ (0·7071–0·7074; Fig. 4) throughout MZ$_U$ and UZ compared with the large spread in Sr isotope compositions measured in the rest of the Bushveld Complex (Sr$_0$, 0·7045–0·7090; Kruger, 1994) suggests an internal mechanism for generation of this layered sequence. We also note that exactly the same Sr$_0$ value was obtained for the MZ$_U$ and UZ in the eastern limb (Sharpe, 1985), although his interpretation was different from ours. No isotope data are available for the northern limb. The Sr$_0$ data for the eastern and western limbs imply that the entire magma sheet must have been isotopically homogeneous subsequent to the magma mixing event that resulted in the formation of the Pyroxenite Marker (Kruger *et al.*, 1987; Cawthorn *et al.*, 1991). Further, the systematic up-section increase in the P_2O_5 content of apatite-free intervals, and a similar smooth up-section decrease of V_2O_5 in magnetite in high-V_2O_5 intervals (Fig. 7) would require a delicate and unlikely balance between the composition and proportions of residual to added magma if magma addition had been the cause. In the following discussion, we, therefore, assume that MZ$_U$ and UZ crystallized from a huge sheet of initially homogeneous magma more than 2 km thick across the eastern and western and possibly northern limbs, i.e. over more than 65 000 km^2.

A comparison of observed and modelled Mg# of clinopyroxene and An% of plagioclase (Fig. 5) indicates that cycle I represents about 40% crystallization of the parental magma. Cycle I is ~330 m thick and this model calculation therefore suggests that it crystallized from a ~800 m thick magma sheet. If the assumption of a 2·1 km thick magma sheet is correct, convection and fractionation in the whole vertical extent of the sheet can be ruled out. We therefore explore the possibility that cycle I crystallized from only a portion of the stratified, sheet-like magma chamber. The assumed starting situation with constant composition and density in the magma above the Pyroxenite Marker is shown in Fig. 9a. We base our physical model on that initially proposed by Jackson (1961, fig. 92) for a vertically extensive magma chamber; namely, that crystallization took place mainly in the lower part of the chamber. His model began with an assumed homogeneous magma chamber, which cooled at the top, and became more dense, but did not crystallize significantly, and began to convect. The effect of the adiabatic gradient relative to the liquidus temperature is that the liquidus is intersected in the basal part of the chamber. In the present case, the crystallization of a gabbronoritic mineral assemblage produces a residual liquid with raised density, which would not circulate back to the top but would pond at the base, producing a stable density profile. As a result of slower diffusion of major elements relative to heat, such a magma sheet might separate into double-diffusive convective layers (McBirney & Noyes, 1979) as illustrated in a vertical slice of the Bushveld magma sheet (Fig. 9b). This situation is stable as long as the density of the residual magma increases during crystallization. This scenario changes dramatically in the upper part of cycle I (UZa) once magnetite began to crystallize. The forward model predicts that crystallization of magnetite gabbronorite lowers the density of the magma near the base of the chamber. Eventually, the density of this basal magma layer becomes equal to that of the overlying layer resulting in mixing, as depicted in Fig. 9c. A consequence of this bottom crystallization is that the basal magma layer becomes the most compositionally evolved, as illustrated by Mg# in Fig. 9b. The mixing event, therefore, produces a somewhat more primitive magma composition at the crystallization front (Fig. 9c). We, therefore, suggest that the reversal to higher Mg# of clinopyroxene and higher An% of plagioclase between cycles I and II (Fig. 4) can be explained by mixing between the two lowermost magma layers in the chamber. Magnetite gabbronorite now crystallizes, to be joined after a further small degree of fractionation by olivine. Crystallization of such iron-rich cumulates drives

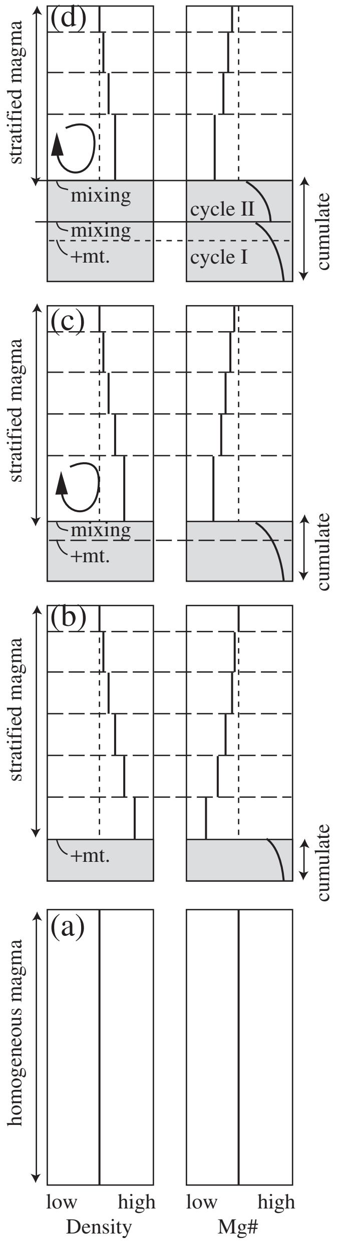

Fig. 9. Magma chamber model for the lower cycles of MZ_U and UZ showing schematically the density and composition (Mg#) of magma and cumulates in a vertical slice of the Bushveld magma sheet. (a) This diagram shows the starting situation, with a thick, homogeneous magma sheet assumed to result from magma recharge and complete mixing at the Pyroxenite Marker. (b) During crystallization of MZ_U gabbronorite at the bottom of the magma chamber, the density of the residual magma increases (and Mg# decreases), resulting in a stable density profile within the magma sheet that is then likely to break into double-diffusive layers. The illustration shows the situation at the time the first magnetite crystallizes. (c) Here the crystallization front has advanced by crystallizing magnetite gabbronorite (UZa), resulting in a decrease of magma Mg# and a decrease in magma density. The diagram illustrates the instant when the density in the lowermost layer equals that of the overlying layer, resulting in complete mixing of the two layers. (d) This diagram illustrates the mixing event resulting in the reversal in mineral compositions between cycles II and III.

the residual magmas to lower density, ultimately causing the bottom two magma layers to mix, terminating cycle II. The increase of plagioclase An% to 58 in the upper half of cycle II (at 1437 m, Fig. 4) indicates the presence of at least one further cycle at this level, although this cannot be resolved firmly by the present dataset. The mixed magma at the base of cycle III is slightly more primitive than the parent magma to the upper half of cycle II, such that it no longer crystallizes olivine, but produces magnetite gabbronorite. The disappearance of olivine is explained by this process, although it reappears in the middle of cycle III as a result of fractionation. Further crystallization of olivine- and magnetite-bearing assemblages continues to drive the magma to lower density, resulting in periodic magma mixing events, as depicted in Fig. 9d. Cycles III–V are particularly well-developed in the Bierkraal drill core (Fig. 4). In the ~300 m thick cycle V, for example, the up-section change in An% is from 55 to 46, the $Mg\#_{cpx}$ changes from 58 to 26 and olivine changes from Fo_{52} to Fo_{6} (Fig. 4). A forward model calculation of fractional crystallization similar to the model presented above (not shown) suggests that cycle V represents about 50% crystallization and therefore indicates that the magma layer undergoing fractionation was ~600 m thick.

The variations in V content of magnetite demonstrate overall fractionation through the entire Upper Zone. However, in detail, the changes are extremely difficult to model. The partition coefficient for V between clinopyroxene and melt ranges from 1 to 3, depending upon fO_2 (Toplis & Corgne, 2002). Smaller values are expected for orthopyroxene. Thus, in magnetite-free gabbronorite cumulates the bulk partition coefficient will be less than or close to unity, and so small degrees of fractionation will have little effect upon the V content of the evolving melt. However, for magnetite the partition coefficient ranges from 10 to 40, decreasing with oxidation (Toplis & Corgne, 2002). Hence, the presence of 10%, or more, of magnetite in the crystallizing assemblage will result in a bulk partition coefficient significantly greater than unity, leading to a decrease in V in the melt and in subsequent magnetite. However, quantitative modeling of the trend seen in Fig. 7 is not possible because the value of fO_2 is not known, and, more importantly, we do not know whether it remains constant or responds to periods of excessive magnetite formation (as seen in the thick layers). For example, if the fO_2 of the melt is reduced by removal of excessive magnetite, the partition coefficient into magnetite would increase and the abundance of V in subsequent magnetite might increase even though the abundance of V in the melt might be decreasing. Because of such variation in the partition coefficient as a result of changes in fO_2 it is not permissible to conclude that an increase in V in magnetite indicates addition of less evolved magma.

The high-field strength element phosphorus is particularly useful as a tracer of crystallization processes in mafic cumulates. It is almost perfectly excluded from silicate minerals, but is a major component of apatite. When apatite becomes a liquidus phase at about 1% P_2O_5 in a basic melt (Green & Watson, 1982), the cumulate rock contains more P than the melt, which is therefore gradually depleted in P (Wager, 1960). Because P is an essential component of apatite, the depletion of P in the magma results in a decrease in the amount of apatite that can crystallize at the cotectic. This is demonstrated, for example, in the apatite mode and P_2O_5 variations of the Skaergaard intrusion (Wager, 1963).

Apatite is locally abundant in cycles IV–IX (UZc) and occurs intermittently throughout the stratigraphic section (Fig. 7). At the bases of cycles V and VI, which are defined by breaks in mineral compositions (Figs 4 and 7b), there are 60–70 m thick, low-P_2O_5 intervals where cumulus apatite is absent (Fig. 7a). Apatite may have been removed from the liquidus by mixing with apatite-undersaturated magma. The return of abundant liquidus apatite 60–70 m above the bases of these cycles (Fig. 7a) is the result of simple fractional crystallization driving the magma back to apatite saturation. In the upper half of the UZ, we interpret low-P_2O_5 intervals lacking cumulus apatite as evidence for magma mixing events (Fig. 7a). We have, therefore, placed cycle boundaries at the levels where cumulus apatite disappears, i.e. where the P_2O_5 content abruptly decreases below 1 wt %. In these uppermost cycles the intervals lacking apatite become thinner upwards, indicating that apatite was only briefly removed from the liquidus. This could explain the lack of significant breaks in An% and $Mg\#_{cpx}$ at these levels (Fig. 4), although it is possible that closer sampling could reveal subtle changes in An% and Mg#. In cycle IV, where cumulus apatite first appears and defines the base of UZc (Fig. 4), there are two short high-P_2O_5 intervals interbedded with the low-P_2O_5 succession (Fig. 7a). These high-P_2O_5 intervals occur in rocks enriched in magnetite and olivine. This association of apatite could possibly relate to physical sorting of dense cumulus minerals or fluctuations in the solubility of P in the magma (Green & Watson, 1982) but a firm explanation must await a detailed study of closely spaced samples. The smooth up-section increase in P_2O_5 in the low-P_2O_5 intervals (Fig. 7a), and the smooth decrease in V_2O_5 in the high-V_2O_5 intervals (Fig. 7b), support a model involving crystallization and mixing within a stratified magma sheet. It would appear fortuitous if recharge from an extraneous magma source produced such systematic trends.

Formation of magnetitite and nelsonite layers

The magnetitite and nelsonite layers of the UZ contain important orthomagmatic deposits of vanadium, titanium and phosphorus (Lee, 1996; von Gruenewaldt, 1993; Cawthorn *et al.*, 2005). The formation of the massive magnetitite layers (Fig. 3f) has been variably explained, as follows.

(1) Bateman (1951) suggested that an iron-rich immiscible liquid might have separated and produced magnetite-rich layers. This concept has been applied to the Bushveld Complex by Reynolds (1985*a*) and von Gruenewaldt (1993). We would argue that a very dense, low-viscosity immiscible, iron-rich liquid might be expected to percolate downwards through the underlying plagioclase-rich crystal mush, and not produce the remarkably planar bases commonly observed (Fig. 3f). Further, immiscible iron-rich liquids contain only about 30% total FeO (Jakobsen *et al.*, 2005), and so a further process is required to produce the near-monomineralic magnetitite layers from such a liquid (Cawthorn *et al.*, 2005).

(2) The sinking and sorting of dense magnetite grains was proposed by Wager & Brown (1968). However, they noted that there is a significant inconsistency; namely, that pyroxenes are absent in magnetite-anorthosite sequences (e.g. Fig. 3f). Had the magma simply evolved to magnetite saturation, a gravity-controlled succession ought to include pyroxene between the magnetite and anorthosite layers. Some additional mechanism would appear to be required to cause pyroxene to cease crystallization.

(3) The possibility of the formation of chromitite layers as a result of magma addition and mixing (Irvine, 1975) has been extrapolated to the formation of magnetitite layers (Harney *et al.*, 1990), although appropriate phase diagrams have not been presented. Ashwal *et al.* (2005) documented reversals in Mg# of pyroxene and An% of plagioclase in a drill core through the MZ_U and UZ in the northern limb, which they interpreted as evidence for magma recharge. As discussed above, we disagree with this interpretation for the Bierkraal drill core through the western limb.

(4) Increase in fO_2 in the magma by fluids derived from the country rocks has been proposed as a way to induce magnetite saturation (Klemm *et al.*, 1985; von Gruenewaldt *et al.*, 1985). The source, and mechanism of addition, of such fluid remains to be demonstrated. Furthermore, the lateral continuity of the magnetitite layers requires a process that can operate simultaneously throughout the entire magma chamber.

(5) By analogy with the formation of chromitite layers as a result of pressure increase (Lipin, 1993), an increase in pressure exerted on magma can induce magnetite saturation (Cawthorn & McCarthy, 1980). Physical processes causing such pressure changes need to be established, but have been proposed by Lipin (1993) and Carr *et al.* (1994).

(6) In contrast to the crystal-settling concept, Cawthorn & McCarthy (1980) used the cyclicity in Cr contents across massive magnetitite layers as evidence for crystallization at the base of the magma chamber. Reversals in Cr content of magnetite resulted from diffusion from the overlying magma. A slightly different interpretation for these data was given by Kruger & Smart (1987), who suggested that crystallization occurred within a basal layer of magma that underwent periodic mixing with overlying layers within a stratified chamber. Similarly, Harney *et al.* (1996) interpreted changes in Sr/Al_2O_3 of plagioclase separates taken across the Main Magnetitite Layer as evidence of mixing as a result of the breakdown of stratified magma layers caused by density inversion during the crystallization of magnetitite layers.

The positions of the 32 magnetitite and nelsonite layers (Table 2; Fig. 4) relative to the cycles described above throw new light on their petrogenesis. The basal package of magnetitite layers includes eight layers that range from 26 to 246 cm in thickness, totalling 731 cm, and are distributed between 1839 and 1719 m in the stratigraphy (Table 2; Fig. 4). Of these, the 246 cm thick Main Magnetitite Layer is the lowest at 1839 m. This occurs some 50–100 m below the interval (1781–1739 m) displaying a reversal in An% of plagioclase between cycles I and II (Fig. 4; Table 3). Two other magnetitite layers also occur below the Reversal in An%. Few layers occur within the reversal and the uppermost magnetitite layer in this package is located 20 m above the top of the reversal (Tables 2 and 3). Based on much more detailed sample spacing, it was shown by Fox (1982) and Harney *et al.* (1996) that the Main Magnetitite Layer at Magnet Heights in the eastern limb, likewise, is not associated with a reversal in An% (Fig. 6). In the upper part of cycle II there is a package of three magnetitite layers between 1441 and 1427 m, totalling 113 cm in thickness (Table 2). These layers are not related to a significant reversal in mineral compositions (Fig. 4). In cycle III, an 80 cm thick magnetitite layer occurs in a section displaying rapidly declining An% (Fig. 4). Between 1020 and 945 m there is another package including 12 magnetitite layers totalling 1045 cm in thickness (Table 2; Fig. 4). The reversal interval between cycles IV and V is placed at 998–981 m and shows pronounced changes in plagioclase, clinopyroxene, olivine and magnetite compositions (Figs 4 and 7b). Similar to the magnetitite layers straddling the boundary between cycles I and II, these magnetitite layers occur below, within, and above the regressive interval between cycles IV and V. It is noteworthy that this package of magnetitite layers coincides with a low-P_2O_5 interval (Fig. 7a). Of the uppermost eight oxide-rich layers, six are nelsonites and they all occur within cycles and not at their boundaries (Fig. 4). We, therefore, conclude that simple fractional crystallization led to the formation of the magnetitite layers.

The broad coincidence of the most significant packages of magnetitite layers with the boundaries between cycles I–II and IV–V, however, suggests a relationship. In both cases, thick magnetitite layers occur just below the reversals in mineral compositions and formed as a result of normal fractional crystallization. The crystallization of such thick magnetitite layers must have lowered the density of the residual magma dramatically. We, therefore, suggest that the formation of the basal magnetitite layers in these two packages accelerated the trend of density decrease and initiated magma mixing and the formation of a mineralogical reversal. We further speculate that the occurrence of several, closely spaced magnetitite layers in these reversal intervals resulted from magma inhomogeneity during a single mixing event, perhaps a result of finger instability during mixing between two magma layers (Irvine *et al.*, 1983). In several cases, magnetitite and nelsonite layers occur within cycles (Fig. 4) and are apparently not related to reversals. Most of these magnetitite layers are relatively thin and single (Table 2). We explain these magnetitite layers as the result of normal fractional crystallization.

Apatite becomes a liquidus phase and coprecipitates with magnetite in the nelsonite layers in cycles V–IX (Figs 3e and 4), suggesting that they formed as a consequence of fractional crystallization. Fe–P–Ti-rich immiscible liquids exsolved during late-stage fractional crystallization in the Skaergaard intrusion (Jakobsen *et al.*, 2005), and by analogy this implies that immiscibility is also possible in the evolved stages of the Bushveld Complex. However, we prefer to envisage a single mechanism that produced all the magnetite-rich layers, rather than appealing to liquid immiscibility for the upper, apatite-bearing layers [as suggested by Reynolds (1985*a*) and von Gruenewaldt (1993)], and a different process for the lower apatite-free layers.

Comparison with eastern and northern limbs of the Bushveld Complex

The studied sections of UZ are broadly similar in the three major limbs (von Gruenewaldt, 1973; Molyneux, 1974; Ashwal *et al.*, 2005; this study). The thicknesses vary from 1510 to 2230 m (Table 1) and they are subdivided into three subzones defined by the first appearance of cumulus magnetite, olivine and apatite, respectively. Above, we have shown for the Bierkraal section, however, that the presence of cumulus olivine and apatite is intermittent (Figs 4c and 7a) and that this has important petrogenetic implications. The reported intervals of occurrence of olivine in UZb + c and apatite in UZc in the eastern (von Gruenewaldt, 1973) and northern limbs (Ashwal *et al.*, 2005) are, therefore, summarized in Fig. 10. This figure shows that olivine and apatite are intermittent in all three limbs. The presence of cumulus olivine in the Bellevue core of the northern limb broadly corresponds to intervals showing normal fractionation trends (Ashwal *et al.*, 2005). Furthermore, the two main intervals displaying a reversal in An% of plagioclase and Mg# of the mafic silicates in UZ occur at 720–640 m and 420–330 m depth in the Bellevue core and coincide with gaps in the presence of cumulus olivine (Ashwal *et al.*, 2005). The interval in UZc lacking in apatite in the Bellevue core (430–300 m depth; Ashwal *et al.*, 2005) overlaps with the interval where olivine is absent. Many of the mineral compositional data presented above are comparable with similar results obtained for the other limbs of the Bushveld Complex. In the eastern limb, von Gruenewaldt (1973) and Molyneux (1974) provided mineral compositional data for the Main and Upper Zones, although some of their data were obtained by optical and X-ray diffraction methods, rather than by electron microprobe. Also, no compositional data are available for the clinopyroxene. Ashwal *et al.* (2005) provided electron microprobe data for a very large number of samples through part of the Main Zone and the entire Upper Zone for the northern limb. In general, the order of appearance of minerals is very similar in

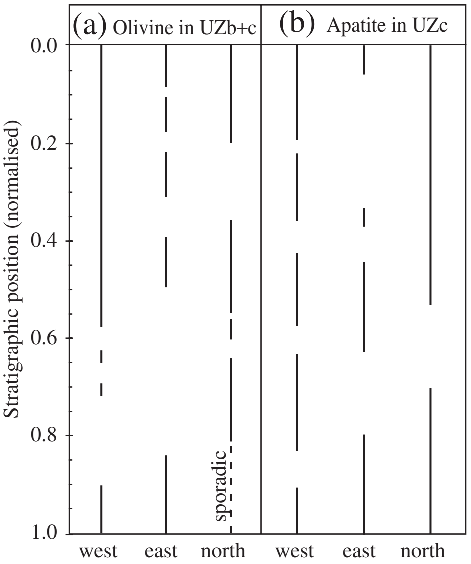

Fig. 10. Distribution of (a) cumulus olivine in UZb + c and (b) apatite in UZc, in the northern (Bellevue core; Ashwal *et al.*, 2005), eastern (field relations; von Gruenewaldt, 1973) and western (this study) limbs of the Bushveld Complex.

all limbs, although two differences exist in the northern limb compared with the eastern and western. An orthopyroxene-rich layer with reversal in composition (i.e. the Pyroxenite Marker) has not been identified in the northern limb. Also, Ashwal *et al.* (2005) suggested that apatite appears 100 m lower in the succession than olivine, but it is transitory and does not reappear for a further 400 m. In all limbs considerable oscillation of mineral compositions occurs, superimposed on the overall fractionation trends. The actual mineral compositions at which the different phases appear are slightly different, although detailed comparison is hampered by the different analytical methods used, the considerable small-scale vertical variation in composition, and irregular spacing of the data points.

The magma chamber model developed above (Fig. 9), therefore, provides a possible explanation for the cyclicity observed in all the limbs. The 2–3 m thick Main Magnetitite Layer and the 7–13 m thick layer (called Layer 21 in the eastern limb) are unequivocally identifiable in the three limbs. Ashwal *et al.* (2005) identified 32 magnetitite layers in the northern limb, which can possibly be grouped into four packages. In the eastern limb only 26 layers are reported (Willemse, 1969*b*; Molyneux, 1974), again in four intervals, but this information is based on field observations; a continuous borehole may reveal additional magnetitite layers. The grouping of the 32 layers identified in this study (Fig. 4, Table 2) is less definitive. Further, we note the absence of layers below the Main Magnetitite Layer in our study, contrasting with three and two layers in the eastern and northern limbs, respectively. There are also a greater number of layers (eleven) in this study above the very distinctive 7 m thick layer 21 (Table 2) compared with the northern (three) and eastern (none) limbs. We suggest that considerable similarities exist in the magnetitite layers between all limbs, but perfect correlation is not possible. Hence, the number of cycles and the proposed mechanism by which they are generated may not be an instantaneous chamber-wide process, but merely an inevitable consequences of crystallization of magnetite at the base of a stratified magma sheet.

CONCLUSIONS

New mineral chemical data for plagioclase, pyroxene, olivine, and magnetite, and whole-rock P_2O_5 and Sr isotope data for the upper Main Zone and Upper Zone in the Bierkraal drill core of the western Bushveld Complex show the following features.

(1) Existing and new initial $^{87}Sr/^{86}Sr$ values are near-constant ($0{\cdot}7073 \pm 0{\cdot}0001$, $n = 22$), suggesting crystallization from a homogeneous magma sheet without major magma recharge or assimilation.

(2) The mafic rocks evolve up-section from gabbronorite (plagioclase An_{72}; clinopyroxene Mg# 74) at the Pyroxenite Marker to magnetite–ilmenite–apatite–fayalite ferrodiorite (An_{43}; Mg#$_{cpx}$ 5; Fo_1 olivine) at the roof of the mafic complex.

(3) The overall fractionation trend is, however, interrupted by reversals to higher An% of plagioclase, Mg# of pyroxene and olivine, V_2O_5 in magnetite, and/or intermittent absence of cumulus apatite or olivine. These reversals define at least nine major fractionation cycles that range from 100 to 400 m in thickness.

(4) We have estimated a plausible magma composition that existed in the chamber at the level of the Pyroxenite Marker, based on summation of rock compositions above that level, plus the addition of postulated expelled magma during final crystallization. It has the composition of a slightly quartz-normative, iron-rich tholeiite.

(5) Forward modeling of fractional crystallization using this composition predicts increasing FeO (total), near-constant SiO_2 and increasing density of the residual magma before magnetite crystallizes, and increasing SiO_2, near-constant FeO and decreasing magma density after magnetite crystallizes. When olivine reappears as a cumulus phase, the FeO content and density of melt decrease.

(6) We explain the observed cyclicity by crystallization at the floor of a huge, stratified magma sheet more than 2 km thick, covering at least 65 000 km^2. Magma stratification with a stable density profile initially developed during crystallization of gabbronorites in the upper Main Zone from a basal layer of magma. Once magnetite began to crystallize, the magma density decreased and periodic density inversion led to mixing with the overlying magma layer, producing mineralogical breaks between fractionation cycles.

(7) The investigated section includes 26 magnetitite and six nelsonite (magnetite–ilmenite–apatite) layers that mainly occur within fractionation cycles. In at least two cases, crystallization of thick magnetitite layers may have lowered the magma density sufficiently to trigger density inversion, resulting in near-coincidence of mineralogical breaks and packages of magnetitite layers.

ACKNOWLEDGEMENTS

This research was supported by grants from the Danish Natural Science Research Council and the National Research Foundation of South Africa and the Angloplats, Implats and Lonplats mining companies. The Council for Geosciences, South Africa, is thanked for access to the Bierkraal core material and permission to publish. We thank Richard Wilson, Jean-Clair Duchesne, Tony Morse, Chris Harris and Marjorie Wilson for critical comments and discussions.

SUPPLEMENTARY DATA

Supplementary data for this paper are available at *Journal of Petrology* online.

REFERENCES

Ariskin, A. A., Frenkel, M. Y., Barmina, G. S. & Nielsen, R. L. (1993). Comagmat: a Fortran program to model magma differentiation processes. *Computers & Geosciences* **19**, 1155–1170.

Ashwal, L. D., Webb, S. J. & Knoper, M. W. (2005). Magmatic stratigraphy in the Bushveld northern lobe: continuous geophysical and mineralogical data from the 2950 m Bellevue drillcore. *South African Journal of Geology* **108**, 199–232.

Atkins, F. B. (1969). Pyroxenes of the Bushveld Intrusion, South Africa. *Journal of Petrology* **10**, 222–249.

Barnes, S. J. (1986). The effect of trapped liquid crystallization on cumulus mineral compositions in layered intrusions. *Contributions to Mineralogy and Petrology* **93**, 524–531.

Bateman, A. M. (1951). The formation of late magmatic oxide ores. *Economic Geology* **46**, 404–426.

Buick, I. S., Maas, R. & Gibson, R. (2001). Precise U–Pb titanite age constraints on the emplacement of the Bushveld Complex, South Africa. *Journal of the Geological Society, London* **158**, 3–6.

Carr, H. W., Groves, D. I. & Cawthorn, R. G. (1994). The importance of synmagmatic deformation in the formation of Merensky Reef potholes in the Bushveld Complex. *Economic Geology* **89**, 1398–1410.

Cawthorn, R. G. & McCarthy, T. S. (1980). Variations in Cr content of magnetite from the Upper Zone of the Bushveld Complex—evidence for heterogeneity and convection currents in magma chambers. *Earth and Planetary Science Letters* **46**, 335–343.

Cawthorn, R. G. & McCarthy, T. S. (1985). Incompatible trace element behavior in the Bushveld Complex. *Economic Geology* **80**, 1016–1026.

Cawthorn, R. G. & Molyneux, T. G. (1986). Vanadiferous magnetite deposits of the Bushveld Complex. In: Anhaeusser, C. R. & Maske, S. (eds) *Mineral Deposits of South Africa*. Johannesburg: Geological Society of South Africa, pp. 1251–1266.

Cawthorn, R. G. & Walraven, F. (1998). Emplacement and crystallization time for the Bushveld Complex. *Journal of Petrology* **39**, 1669–1687.

Cawthorn, R. G. & Walsh, K. L. (1988). The use of phosphorus contents in yielding estimates of the proportion of trapped liquid in cumulates of the Upper Zone of the Bushveld Complex. *Mineralogical Magazine* **52**, 81–89.

Cawthorn, R. G. & Webb, S. J. (2001). Connectivity between western and eastern limbs of the Bushveld Complex. *Tectonophysics* **330**, 195–209.

Cawthorn, R. G., Meyer, P. S. & Kruger, F. J. (1991). Major addition of magma at the Pyroxenite Marker in the western Bushveld Complex, South Africa. *Journal of Petrology* **32**, 739–763.

Cawthorn, R. G., Barnes, S. J., Ballhaus, C. & Malitch, K. N. (2005). Platinum-group element, chromium, and vanadium deposits in mafic and ultramafic rocks. *Economic Geology, 100th Anniversary Volume*, pp. 215–249.

Coffin, M. F. & Eldholm, O. (1994). Large igneous provinces: crustal structure, dimensions, and external consequences. *Reviews of Geophysics* **32**, 1–36.

Eales, H. V. & Cawthorn, R. G. (1996). The Bushveld Complex. In: Cawthorn, R. G. (ed.) *Layered Intrusions*. Amsterdam: Elsevier, pp. 181–230.

Eales, H. V., de Klerk, W. J., Butcher, A. R. & Kruger, F. J. (1990). The cyclic unit beneath the UG1 chromitite (UG1FW unit) at RPM Union Section Platinum Mine—Rosetta Stone of the Bushveld Upper Critical Zone? *Mineralogical Magazine* **54**, 23–43.

Fox, N. (1982). Variation in plagioclase compositions across magnetitite layers in the eastern Bushveld Complex. University of Cape Town, Honours thesis.

Ghiorso, M. S. & Sack, R. O. (1995). Chemical mass transfer in magmatic processes IV. A revised and internally consistent thermodynamic model for the interpolation and extrapolation of liquid–solid equilibria in magmatic systems at elevated temperatures and pressures. *Contributions to Mineralogy and Petrology* **119**, 197–212.

Green, T. H. & Watson, E. B. (1982). Crystallization of apatite in natural magmas under high pressure hydrous conditions, with particular reference to 'orogenic' rock series. *Contributions to Mineralogy and Petrology* **79**, 96–105.

Harney, D. M. W., Merkle, R. K. W. & von Gruenewaldt, G. (1990). Platinum-group element behavior in the lower part of the Upper Zone, Eastern Bushveld Complex—implications for the formation of the main magnetite layer. *Economic Geology* **85**, 1777–1789.

Harney, D. M. W., von Gruenewaldt, G. & Merkle, R. K. W. (1996). The use of plagioclase composition as an indicator of magmatic processes in the Upper Zone of the Bushveld Complex. *Mineralogy and Petrology* **56**, 91–103.

Hunter, R. H. & Sparks, R. S. J. (1987). The differentiation of the Skaergaard Intrusion. *Contributions to Mineralogy and Petrology* **95**, 451–461.

Irvine, T. N. (1975). Crystallization sequences in the Muskox intrusion and other layered intrusions. 2. Origin of chromitite layers and similar deposits of other magmatic ores. *Geochimica et Cosmochimica Acta* **39**, 991–1008.

Irvine, T. N., Keith, D. W. & Todd, S. G. (1983). The J-M Platinum–Palladium Reef of the Stillwater Complex, Montana: II. Origin by double-diffusive convective magma mixing and implications for the Bushveld Complex. *Economic Geology* **78**, 1287–1334.

Jackson, E. D. (1961). *Primary T|extures and Mineral Associations in the Ultramafic Zone of the Stillwater Complex, Montana. US Geological Survey, Professional Papers* **358**.

Jakobsen, J. K., Veksler, I. V., Tegner, C. & Brooks, C. K. (2005). Immiscible iron- and silica-rich melts in basalt petrogenesis documented in the Skaergaard intrusion. *Geology* **33**, 885–888.

Klemm, D. D., Henckel, J., Dehm, R. & von Gruenewaldt, G. (1985). The geochemistry of titanomagnetite in magnetite layers and their host rocks of the Eastern Bushveld Complex. *Economic Geology* **80**, 1075–1088.

Kretz, R. (1963). Distribution of magnesium and iron between orthopyroxene and calcic pyroxene in natural mineral assemblages. *Journal of Geology* **71**, 773–785.

Kruger, F. J. (1994). The Sr-isotopic stratigraphy of the western Bushveld Complex. *South African Journal of Geology* **97**, 393–398.

Kruger, F. J. (2005). Filling the Bushveld Complex magma chamber: lateral expansion, roof and floor interaction, magmatic unconformities, and the formation of giant chromitite, PGE and T-V-magnetitite deposits. *Mineralium Deposita* **40**, 451–472.

Kruger, F. J. & Smart, R. (1987). Diffusion of trace elements during bottom crystallization of double-diffusive convection systems: the magnetitite layers of the Bushveld Complex. *Journal of Volcanology and Geothermal Research* **34**, 133–142.

Kruger, F. J., Cawthorn, R. G. & Walsh, K. L. (1987). Strontium isotopic evidence against magma addition in the Upper Zone of the Bushveld Complex. *Earth and Planetary Science Letters* **84**, 51–58.

Lee, C. A. (1996). A review of mineralizations in the Bushveld Complex and some other layered intrusions. In: Cawthorn, R. G. (ed.) *Layered Intrusions*. Amsterdam: Elsevier, pp. 103–145.

Lipin, B. R. (1993). Pressure increase, the formation of chromitite layers and the development of the Ultramafic Series in the Stillwater Complex. *Journal of Petrology* **34**, 955–976.

Lundgaard, K. L., Tegner, C., Cawthorn, R. G., Kruger, F. J. & Wilson, J. R. (1993). Trapped intercumulus liquid in the Main Zone of the eastern Bushveld Complex, South Africa. *Contributions to Mineralogy and Petrology* **151**, 352–369.

McBirney, A. R. (1993). *Igneous Petrology. 2nd edn*. Boston, MA: Jones & Bartlett, pp. 508.

McBirney, A. R. & Noyes, M. N. (1979). Crystallization and layering of the Skaergaard intrusion. *Journal of Petrology* **20**, 487–554.

Merkle, R. K. W. & von Gruenewaldt, G. (1986). Compositional variation of Co-rich pentlandite: relation to the evolution of the Upper Zone of the western Bushveld Complex, South Africa. *Canadian Mineralogist* **24**, 529–546.

Mitchell, A. A., Eales, H. V. & Kruger, F. J. (1998). Magma replenishment, and the significance of poikilitic textures, in the Lower Main Zone of the western Bushveld Complex, South Africa. *Mineralogical Magazine* **62**, 435–450.

Molyneux, T. G. (1972). X-ray data and chemical analyses of some titanomagnetite and ilmenite samples from the Bushveld Complex, South Africa. *Mineralogical Magazine* **48**, 863–871.

Molyneux, T. G. (1974). A geological investigation of the Bushveld Complex in Sekhukhuneland and part of the Steelpoort valley. *Transactions of the Geological Society of South Africa* **77**, 329–338.

Morse, S. A. (1984). Cation diffusion in plagioclase feldspar. *Science* **225**, 504–505.

Nex, P. A., Kinnaird, J. A., Ingle, L. J., Van der Vyver, B. A. & Cawthorn, R. G. (1998). A new stratigraphy for the Main Zone of the Bushveld Complex, in the Rustenburg area. *South African Journal of Geology* **101**, 215–223.

Reynolds, I. M. (1985a). The nature and origin of titaniferous magnetite-rich layers in the Upper Zone of the Bushveld Complex: a review and synthesis. *Economic Geology* **80**, 1089–1108.

Reynolds, I. M. (1985b). Contrasted mineralogy and textural relationships in the uppermost titaniferous magnetite layers of the Bushveld Complex in the Bierkraal area north of Rustenburg. *Economic Geology* **80**, 1027–1048.

Sharpe, M. R. (1985). Strontium isotope evidence for preserved density stratification in the Main Zone of the Bushveld Complex. *Nature* **316**, 119–126.

Spulber, S. D. & Rutherford, M. J. (1983). The origin of rhyolite and plagiogranite in oceanic crust: an experimental study. *Journal of Petrology* **24**, 1–25.

Tegner, C. (1997). Iron in plagioclase as a monitor of the differentiation of the Skaergaard intrusion. *Contributions to Mineralogy and Petrology* **128**, 45–51.

Tegner, C., Robins, B., Reginiussen, H. & Grundvig, S. (1999). Assimilation of crustal xenoliths in a basaltic magma chamber: Sr and Nd isotopic constraints from the Hasvik Layered Intrusion, Norway. *Journal of Petrology* **40**, 363–380.

Toplis, M. J. (2005). The thermodynamics of iron and magnesium partitioning between olivine and liquid: criteria for assessing and predicting equilibrium in natural and experimental systems. *Contributions to Mineralogy and Petrology* **149**, 22–39.

Toplis, M. J. & Carroll, M. R. (1995). An experimental study of the influence of oxygen fugacity on Fe–Ti oxide stability, phase relations, and mineral–melt equilibria in ferro-basaltic systems. *Journal of Petrology* **36**, 1137–1170.

Toplis, M. J. & Corgne, A. (2002). An experimental study of element partitioning between magnetite, clinopyroxene and iron-bearing silicate liquids with particular emphasis on vanadium. *Contributions to Mineralogy and Petrology* **144**, 22–37.

Toplis, M. J., Libourel, G. & Carroll, M. R. (1994). The role of phosphorus in crystallization processes of basalt: an experimental study. *Geochimica et Cosmochimica Acta* **58**, 797–810.

Vander Auwera, J. & Longhi, J. (1994). Experimental study of a jotunite (hypersthene monzodiorite): constraints on the parent magma composition and crystallization conditions (P, T, $f\mathrm{O}_2$) of the Bjerkreim–Sokndal layered intrusion (Norway). *Contributions to Mineralogy and Petrology* **118**, 60–78.

von Gruenewaldt, G. (1970). On the phase change orthopyroxene–pigeonite and the resulting textures in the Main and Upper Zones of the Bushveld Complex in the eastern Transvaal. In: Visser, D. J. L. & von Gruenewaldt, G. (eds) *Symposium on the Bushveld Igneous Complex and Other Layered Intrusions*. Johannesburg: Geological Society of South Africa, pp. 67–73.

von Gruenewaldt, G. (1971). A petrological and mineralogical investigation of the rocks of the Bushveld Igneous Complex in the Tauteshoogte–Roossenekal area of the eastern Transvaal. University of Pretoria, , D.Sc. thesis.

von Gruenewaldt, G. (1973). The Main and Upper zones of the Bushveld Complex in the Roossenekal area, Eastern Transval. *Transactions of the Geological Society of South Africa* **76**, 207–227.

von Gruenewaldt, G. (1993). Ilmenite–apatite enrichments in the Upper Zone of the Bushveld Complex: a major titanium-rock phosphate resource. *International Geology Review* **35**, 987–1000.

von Gruenewaldt, G., Klemm, D. D., Henckel, J. & Dehm, R. M. (1985). Exsolution features in titanomagnetites from massive magnetitite layers and their host rocks of the Upper Zone, eastern Bushveld Complex. *Economic Geology* **80**, 1049–1061.

Wager, L. R. (1960). The major element variation of the layered series of the Skaergaard intrusion and a re-estimation of the average composition of the hidden series and of successive residual magmas. *Journal of Petrology* **1**, 364–398.

Wager, L. R. (1963). The mechanism of adcumulus growth in the layered series of the Skaergaard intrusion. In: Fisher, D. J., Frueh, A. J., Hurlbert, C. S. & Tilley, C. E. (eds) *Symposium on Layered Intrusions. Mineralogical Society of America, Special Paper* **1**, 1–9.

Wager, L. R. & Brown, G. M. (1968). *Layered Igneous Rocks*. London: Oliver & Boyd, pp. 572.

Walraven, F. (1987). *Textural, Geochemical and Genetic Aspects of the Granophyric Rocks of the Bushveld Complex. Memoirs of the Geological Survey of South Africa* **72,** 145 pp.

Walraven, F. & Wolmarans, L. G. (1979). Stratigraphy of the upper part of the Rustenburg Layered Suite, Bushveld Complex, in the western Transvaal. *Annals of the Geological Survey of South Africa* **13**, 109–114.

Willemse, J. (1969a). The geology of the Bushveld Igneous Complex, the largest repository of magmatic ore deposits in the world. *Economic Geology Monograph* **4**, 1–22.

Willemse, J. (1969b). The vanadiferous magnetic iron ore of the Bushveld Igneous Complex. *Economic Geology Monograph* **4**, 187–208.